IN-36-CR
19736
P-61

CO_2 Laser Preionisation

Gary D. Spiers

Center for Applied Optics
The University of Alabama in Huntsville
Huntsville
Alabama, 35899

Final Report NASA Contract NAS8-36955
Delivery Order 70

(NASA-CR-184424) CO2 LASER PREIONISATION Final Report, 1990 (Alabama Univ.) 61 p

N93-13797

Unclas

G3/36 0019736

Table of Contents

1 Introduction

This report covers work carried out on NASA contract NAS8-36955 during the year 1990. The report is divided into the following sections:-

Preionisation Review:- A literature survey to identify the required parameters for effective preionisation in TEA CO_2 lasers and the methods and techniques for characterising preionisers.

Cavity Model:- A numerical model of the LP-140 cavity used to determine the cause of the transverse mode stability improvement obtained when the cavity was lengthened.

LP-140 Discharge Characteristics:- The measurement of the voltage and current discharge pulses on the LP-140 and their subsequent analysis resulting in an explanation for the low efficiency of the laser. An assortment of items relating to the development of high-voltage power supplies is also provided. These items are guidelines that were prepared for a GSRP student.

Frequency Chirp:- A program for analysing the frequency chirp data files obtained with the HP time and frequency analyser. A program to calculate the theoretical LIMP chirp is also included and a comparison between experiment and theory is made.

Laser Linewidths:- A program for calculating the CO_2 linewidth and its dependence on gas composition and pressure. The program also calculates the number of axial modes under the FWHM of the line for a given resonator length. A graphical plot of the results is provided.

Appendix (1):- This is a listing of the basic program used to extract the energy deposition rate, impeadance etc. from the discharge voltage and current pulses.

Appendix (2):- Two Mathcad listings, one to calculate arbitrary $TEM_{l,m}$ modes up to 3,3 and the other to calculate the focal length of a thick lens given the radius of curvature of the surfaces. The second document is useful for converting ROC to focal length and vice-versa for the resonator code in section 3.

Appendix (3):- This is a copy of a joint paper between Dr. Jaenisch and myself to be presented at the SPIE High Energy Lasers Conference in Los Angeles on January 24th 1991.

Due to the variety of topics covered an overall conclusion is not provided as each section is self-contained.

2 Preionisation Review

2.1 Introduction

This review is a copy of a document submitted previously, only minor formatting changes have been undertaken. The object of the review was to provide a brief overview of the means of obtaining quantitative data on the relative merits of various preionisation schemes.

The discharge in a TEA CO_2 laser can be divided into three phases, firstly preionisation, which involves the injection of electrons into the gap in which the discharge will be formed. Secondly the application of a high dV/dt voltage pulse to avalanche the preionisation electrons up to an electron concentration suitable for maintaining a stable discharge. The third phase consists of the deposition of energy into the discharge. During this final stage the voltage across the electrodes collapses to a value essentially independent of the driving circuit. Allthough the preionisation pulse can be completed prior to the application of the avalanching pulse, it is more common to arrange the timing such that the avalanching occurs during the peak of the preionisation pulse. This ensures that a minimum number of preionisation electrons are lost to attachment and also limits the degree of avalanching required to form the discharge. The preionisation pulse usually does not continue during the third phase, except for long pulse operation where electrons must be continuously injected into the discharge to maintain its stability. For large cross-section discharges (~10x10 cm^2) the preionisation can not be generated uniformly throughout the discharge gap and so to overcome this, a high preionisation density is created adjacent to one of the electrodes and a weak (non-avalanching) voltage applied across the electrodes to drift this preionisation uniformly through the discharge volume prior to the application of the avalanche voltage. The preionisation of the discharge volume is critical to the successful operation of the discharge and is therefore a vital consideration in the design of a transversely excited gas laser.

2.2 Preionisation requirements

The main requirements of a preionisation source are:-

2.2.1 Large electron production

Theoretical estimates of the minimum preionisation density required for atmospheric pressure discharges range between 10^4-10^6 cm^{-3} [2.1,2.2,2.3,2.4] and experimental verification[2.5] has provided quantitative agreement of these values. The actual discharge has an electron density of 10^{12}-10^{14} cm^{-3} [2.6,2.7,2.8] and experimental evidence[2.5] has shown that initial preionisation densities above the minimum required value will result in more efficient energy extraction from the discharge volume. Additionally with a larger initial electron density less avalanching is required to obtain a stable discharge and a lower initial voltage can be applied to the electrodes.

2.2.2 Uniform electron production

The preionisation must be produced uniformly throughout the discharge to prevent regions of high current density from occuring. This is important as these high current density regions can readily degenerate into arcs.

2.2.3 Efficient electron production

Within the requirements of the LAWS project, only a limited power budget is available and so the efficiency of the preionisation process is important, therefore the number of electrons generated per unit energy input to the preioniser should be as high as possible.

2.2.4 Contaminant free preionisation

The lifetime requirements of the LAWS program requires that the preionisation source should provide little or no contamination that may limit the lifetime of the laser. As an example spark preionisation has in the past been preferred for flowing-gas lasers as it provides large numbers of electrons. However in a sealed laser[2.9,2.10] the high temperature spark results in almost complete dissociation of the CO_2 in the region of the spark resulting in a shorter lifetime for the laser than if a diffuse discharge preionisation source had been used. Additionally the spark pins have a tendency to sputter material onto the main discharge electrodes and the laser optics.

2.3 Preioniser test methods

Traditionally most preionisers have been tested by placing them in a laser and provided the laser has worked the preioniser has been considered satisfactory. There have been very few attempts (in the open literature) to compare preionisers directly. The techniques that have been used to examine the characteristics of preionisers are:-

2.3.1 UHV chamber

A UHV chamber[2.6,2.9-2.15] chamber enables the direct measurement of electron production from the preioniser to be undertaken. Typically a preioniser is placed inside a chamber such that the electrons generated are collected by a very weak electric field across a pair of electrodes. These collection electrodes can be moved to measure the preionisation from various portions of the preioniser. The dependence of the preionisation density on the preioniser drive circuit parameters can obviously be determined using this technique. The signal obtained by this technique for low electron densities is very small (~nV) and considerable care is required in the design of the apparatus. A dummy electrode is utilised to allow a differential signal to be obtained. Additionally suitable filters are normally used to eliminate HF noise which arises from the preionisation discharge. As it has been shown[2.6,2.12,2.16,2.17] that small quantities of organic contaminants can greatly increase the preionisation density for uv based preionisers, to eliminate fluctuations in measurements extreme care must be taken to ensure the cleanliness of the chamber is maintained. By repetitively pulsing the preioniser in the chamber the dependence of the preionisation density on preioniser age could also be determined and after many pulses the gas in the chamber could be analysed to determine the degree of degradation due solely to the preioniser under test. However with the addition of life testing of the preionisers, a high pulse rate becomes desirable to allow the tests to be completed in a reasonable time. This would require cooling and gas circulation within the chamber. From the literature the effect of the preioniser on the gas mixture can easily be determined after ~100,000 pulses (for spark preionisers[2.9,2.10]). If an hour is allowed for this test, this provides for a pulse rate of 28 Hz,which is minimal. As the preionisers are intended to be very clean a pulse rate of 50 Hz may be more suitable.

2.3.2 Photographic studies

Both time-averaged[2.18-2.20] and time resolved[2.18,2.21,2.22] photographic studies have been used to study preionisation and discharge formation. The time averaged studies although of limited value will show regions of very high current density. Time resolved photography provides much more information and can be used to follow the discharge development and enables flaws in the uniformity to be easily seen. The technique requires the use of a streak camera or preferably a framing camera with a resolution ~10-20 nS.

2.3.3 Light Emission

Many of the preionisation schemes rely on the production of uv light which is used to preionise the discharge volume. Measurements have been made of the light production from these preionisers using a photodiode[2.15], however the disadvantage of this technique is that the correlation between light output and electron density, although probably valid, has not been demonstrated.

2.3.4 Microwave interferometry

Early attempts to measure the electron concentrations in a discharge used an X-band microwave interferometer[2.23], however the sensitivity of the device was insufficient and the technique would appear to have been abandoned.

Of the techniques outlined above the UHV chamber is the most important for the quantitative comparison of preionisers. The time averaged photography is relatively easy to accomplish, although ideally a large format camera should be used to ensure adequate resolution. The time resolved photography provides the only means of studying the discharge formation on the preioniser thereby enabling transient 'hot spots', which frequently indicate potential failure locations, to be detected. The microwave interferometer can be discounted due to its limited sensitivity.

2.4 List of required equipment

The equipment ideally required for the characterisation of the preionisers therefore consists of the following items. It should be noted that only a general description is given at this point.

2.4.1 UHV chamber

An UHV chamber assembly consisting of collection electrodes, ports for supplying gas and to enable gas sampling. Suitable feedthroughs for the electrical connections will be required. A large port to which the test preioniser assembly can be fixed and a large transparent window directly opposite this port to enable photography of the preionisation discharge. In order to facilitate movement of the collection electrodes, rotary feedthroughs must be provided if manual adjustment is envisaged. Alternatively and possibly preferably if automatic data collection is required a pair of stepping motors and their associated electronic drivers is required. If life testing is envisaged then gas cooling and recirculation fans must also be supplied.

2.4.2 Drift field power supply

The drift voltage required obviously depends on the electrode spacing but typically a voltage of ~0.3 $Vcm^{-1}torr^{-1}$ is used giving a drift voltage of ~2 kV for an 8 cm gap at atmospheric pressure. Thus a 0-5 kV dc power supply should suffice.

2.4.3 Detection circuitry

This consists primarily of a differential ac amplifier and HF filters (which may be included in some amplifiers). Traditionally the output from the amplifier has been fed to an oscilloscope and displayed so that a photograph of the signal can be obtained. This obviously lends itself to digitisation.

2.4.4 Gas analysis

If the effect of the preionisers on the gas chemistry is to be studied a mass spectrometer will be required.

2.4.5 Time integrated photographic analysis

A suitable large format camera is required.

2.4.6 Time resolved photographic analysis

A suitable high speed framing camera is required.

The above list only covers the equipment required to analyse the electron production from the various preionisers. Thus in addition to this list suitable circuitry for driving the respective preionisers would be required together with high voltage and high current probes for their electrical analysis.

2.5 References

2.1) Palmer, A.J.;"A physical model on the initiation of atmospheric-pressure glow discharges"; Appl. Phys. Lett.; 25; 138 (1974)

2.2) Karnyushin, V.N., A.N. Malov & R.I. Soloukhin;"Influence of preionisation conditions on the development of a homogeneous discharge in gases"; Sov. J. Quant. Electron.; 8; 319 (1978)

2.3) Levatter, J.I. & Shao-Chi Lin;"Necessary conditions for the homogeneous formation of pulsed avalanche discharges at high gas pressures"; J. Appl. Phys.; 51; 210 (1980)

2.4) Gavrilov, P.T., J. Limpouch, G. Loncar, K. Masek & M. Vrbova;"Necessary conditions for the formation of self-sustained discharge in TEA CO_2 lasers"; J. Phys. E: Sci. Instrum.; 20; 906 (1987)

2.5) Suzuki, S., Y. Ishibashi; M. Obara & T. Fujioka;"Dependence of laser output on initial photoelectron density in TEA CO_2 laser"; Appl. Phys. Lett.; 36; 26 (1980)

2.6) Babcock, R.V., I. Liberman & W.D. Partlow;"Volume preionisation from bare sparks"; IEEE J. Quant. Electron.; 12; 29 (1976)

2.7) Kaminski, W.R.;"Corona preionisation technique for carbon dioxide lasers"; UTRC Report B2R-98071-02; United Technology Research Centre (1982)

2.8) Kline, L.E. & L.J. Denes;"Investigations of glow discharge formation with volume preionisation"; J. Appl. Phys.; 46; 1567 (1975)

2.9) Norris,B. & A.L.S. Smith;"Sealed stable TEA CO_2 lasers"; University of St. Andrews; Scotland; Annual Report for CVD Research Project RU16/3 (1977)

2.10) Smith, A.L.S. & B. Norris;"Limiting processes in sealed photoionisation TEA CO_2 lasers"; J. Phys. D: Appl. Phys.; 11; 1949 (1978)

2.11) Yamabe, C., T. Matsushita, S. Sato & K. Horii;"Parametric studies of uv preionisation in TEA CO_2 laser"; J. Appl. Phys.; 51; 898 (1980)

2.12) Scott, S.J. & A.L.S. Smith;"Ultraviolet photoionisation in transversely excited atmospheric CO_2 lasers"; J. Appl. Phys.; 64; 528 (1988)

2.13) Scott, S.J.;"Experimental investigations on an X-ray preioniser test bed"; J. Appl. Phys.; 64; 537 (1988)

2.14) Marchetti, R., E. Penco, E. Armandillo & G. Salvetti;"Optimisation of corona-discharge photoionisation sources for CO_2 lasers"; J. Appl. Phys.; 54; 5672 (1983)

2.15) Marchetti, R., E. Penco & G. Salvetti;"A new type of corona-discharge photoionisation source for gas lasers"; J. Appl. Phys.; 56; 3163 (1984)

2.16) Scott, S.J. & A.L.S. Smith;"Sources of photoionisation in transversely excited atmospheric CO_2 lasers"; Appl. Phys. Lett.; 41; 783 (1982)

2.17) Scott, S.J. & A.L.S. Smith;"Identification of the origins of photoionisation in CO_2 TEA lasers"; Appl. Phys. B; 33; 1 (1984)

2.18) Richardson, M.C., K. Leopold & A.J. Alcock;"Large aperture CO_2 laser discharges"; IEEE J. Quant. Electron.; QE-9; 934 (1973)

2.19) Hasson, V. & H.M. Von Bergmann;"Spatial control of pulsed high-pressure pre-ionisation stabilised glow discharges"; J. Phys. E: Sci. Instrum.; 13; 632 (1980)

2.20) Theophanis, G., & V. Hasson;"X-ray preionised laser development"; AVCO Everett Research Laboratory Inc.; Summary Report (1985)

2.21) Marchetti, R., E. Penco & G. Salvetti;"Ultraviolet preionised CO_2 TEA laser with high output power density utilising non conventional electrode profile"; IEEE J. Quant. Electron.; QE-18; 170 (1982)

2.22) Sakai, Y., M. Takahashi, S. Sakamoto & H. Tagashira;"CO_2 TEA laser discharge development- A high-speed-camera investigation"; J. Appl. Phys.; 50; 647 (1979)

2.23) Seguin, H.J.J., J. Tulip & D. McKen;"UV photoionisation density measurements in TEA lasers"; Appl. Phys. Lett.; 23; 344 (1973)

3 Cavity Model

3.1 Introduction

The transverse mode structure of the laser output pulse is important for obtaining a good far-field beam profile. The initial beam profile of the LP-140 laser had considerable transverse mode instability[3.1]. A schematic of the LP-140 cavity is shown in figure 3.1. Jaenisch[3.1] found that when the cavity length was extended by increasing the seperation between the grating and the lens, the transverse mode stability improved. The model discussed here was developed to provide an explanation for this improvement.

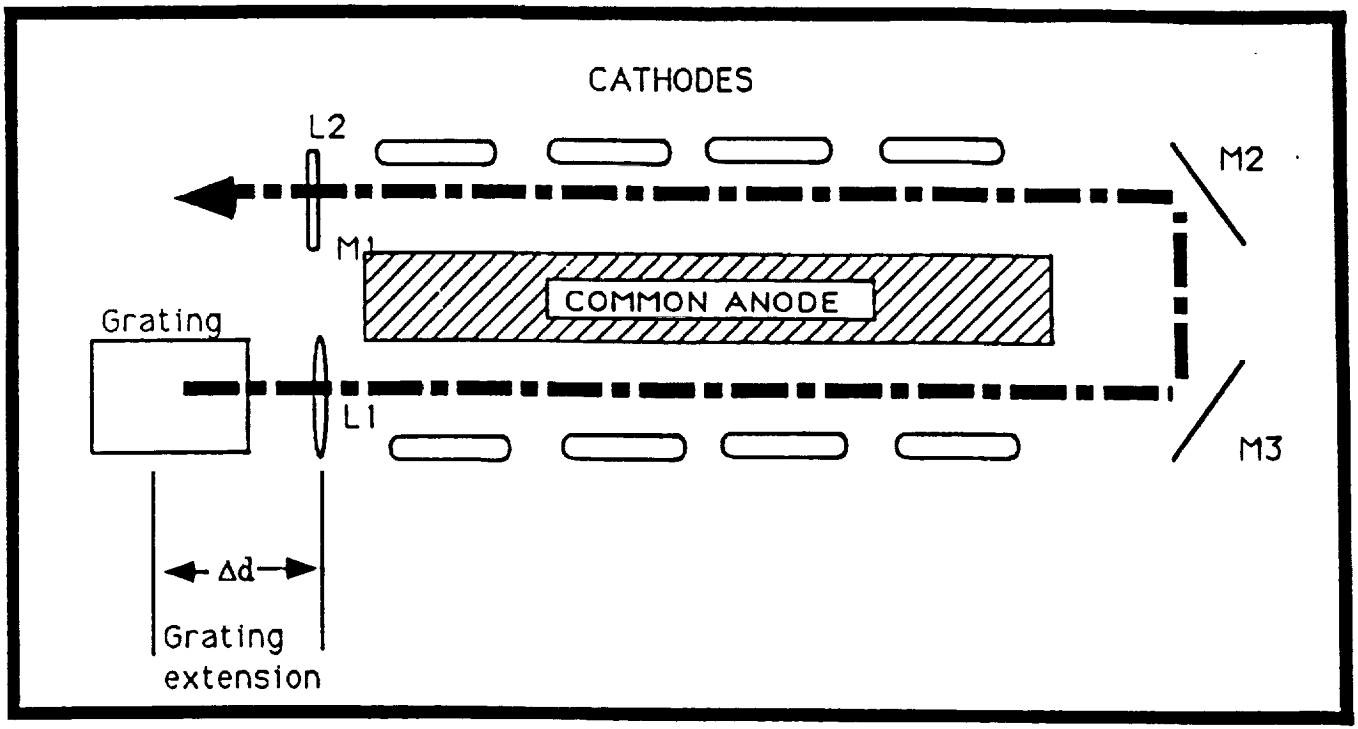

Figure 3.1. The LP-140 cavity layout.

3.2 The matrix model

The model is based on the work of Siegmann[3.2], and has been implemented as a Mathcad[3.3] document. In this model each of the optical elements in the cavity can be expressed as a 2x2 matrix. By combining the matrices a single matrix for the overall optical system can be obtained. From this matrix the magnification and Fresnel numbers of the resonator can be determined.

The simple geometrical magnification of the resonator varies with the complex curvature, q of the input wavefront and for lasing action to occur the wavefront must be capable of reproducing itself over many round trips. This means that the complex curvature of the wavefront after one complete round trip must return to its initial value. This condition constrains the magnification to a single value and it is this value that is calculated by the program.

Rather than provide a detailed theoretical treatise of the model, the reader is referred to the book[3.2] by Siegmann which provides a comprehensive account of the theory. The Mathcad document follows:-

LP-140 CAVITY MODEL

This document uses the matrix method to model the LP-140 cavity. Each of the cavity elements is represented by a matrix where the variables for each matrix are :-

Output coupler radius of curvature (m)	$R1 := -5$
Cavity length between output coupler and lens (m)	$D1 := 2.40$
Radius of curvature of first surface of lens (m)	$R2 := -14.05$
Refractive index of lens material	$N1 := 2.407$
Thickness of lens material (m)	$T1 := 0.00635$
Radius of the second surface of the lens (m)	$R3 := 1000000$
Spacing between the lens and grating (m)	$D2 := 0.1$
Wavelength of laser radiation (m)	$\lambda := 0.0000106$
Mirror diameter (m)	$W := 0.04$
Unstable resonator output coupler half width (m)	$a := 0.009525$
Total cavity length (m)	$LEN := D1 + D2 + T1 \cdot N1$

This provides the following component matrices for one beam direction:-

Output Coupler

$$M_1 := \begin{bmatrix} 1 & 0 \\ \frac{-2}{R1} & 1 \end{bmatrix}$$

Cavity Space

$$M_2 := \begin{bmatrix} 1 & D1 \\ 0 & 1 \end{bmatrix}$$

First surface of lens

$$M_3 := \begin{bmatrix} 1 & 0 \\ \frac{N1 - 1}{R2} & 1 \end{bmatrix}$$

Lens thickness

$$M_4 := \begin{bmatrix} 1 & \frac{T1}{N1} \\ 0 & 1 \end{bmatrix}$$

Second lens surface

$$M_5 := \begin{bmatrix} 1 & 0 \\ \frac{1 - N1}{R3} & 1 \end{bmatrix}$$

Grating Spacing

$$M_6 := \begin{bmatrix} 1 & D2 \\ 0 & 1 \end{bmatrix}$$

Grating

$$M_7 := \begin{bmatrix} 1 & 0 \\ 0 & 1 \end{bmatrix}$$

For the beam travelling in the opposite direction we must reverse the sign of the curvatures on the lens surfaces to give:-

Grating side surface

$$R4 := -R3$$

$$M_{52} := \begin{bmatrix} 1 & 0 \\ \frac{N1 - 1}{R4} & 1 \end{bmatrix}$$

Cavity surface

$$R5 := -R2$$

$$M_{32} := \begin{bmatrix} 1 & 0 \\ \frac{1 - N1}{R5} & 1 \end{bmatrix}$$

The total system matrix is obtained by multiplying out the matrices:-

$$M_s := M_1 \cdot M_2 \cdot M_3 \cdot M_4 \cdot M_5 \cdot M_6 \cdot M_7 \cdot M_6 \cdot M_{52} \cdot M_4 \cdot M_{32} \cdot M_2$$

Giving:-

$$M_s = \begin{bmatrix} 0.504 & 3.765 \\ 0.003 & 2.01 \end{bmatrix}$$

$$|M_s| = 1$$

(This is a check on the validity of the system matrix and should equal 1.)

The ABCD elements of the system matrix are:-

$$A := M_{s_{0,0}} \qquad B := M_{s_{0,1}} \qquad C := M_{s_{1,0}} \qquad D := M_{s_{1,1}}$$

The half trace parameter,m is given by:-

$$m := \frac{A + D}{2}$$

giving $m = 1.257$ (For $-1 < m > 1$ the resonator is unstable, whilst for $-1 < m < 1$ the resonator is stable.)

If the resonator is unstable the magnification is given by:-

$$M := \mathrm{if}\left[m > 1, m + \sqrt{m^2 - 1}, 0\right]$$

$$M := \mathrm{if}\left[m < -1, -m - \sqrt{m^2 - 1}, M\right]$$

i.e. $M = 2.018$(If the magnification has the value 0 this indicates the stable resonator case.)

Now the Fresnel number is calculated for the resonator, together with the collimated and equivalent Fresnel numbers if the resonator is unstable.

Fresnel Number

$$N_f := \frac{W^2}{4 \cdot LEN \cdot \lambda}$$

If unstable then:-

Collimated Fresnel Number

$$N_c := \mathrm{if}\left[M \neq 0, \frac{M \cdot a^2}{B \cdot \lambda}, 0\right]$$

and Equivalent Fresnel Number

$$N_{eq} := \mathrm{if}\left[M \neq 0, \frac{\left[M^2 - 1\right] \cdot N_c}{2 \cdot M^2}, 0\right]$$

The various Fresnel numbers are:-

$N_f = 15.003$ $N_c = 4.587$ $N_{eq} = 1.73$

where a value of zero for the collimated and equivalent Fresnel numbers indicates a stable resonator. These parameters together with the magnification enable a preliminary estimation of the resonator mode stability and losses to be obtained.

3.3 Analysis

The model was run using the initial cavity configuration and then for the cavity as modified by Jaenisch[3.1]. The model was then rerun with the initial cavity length but with a modified prescription for the lens, L1 (figure 3.1). The object of this exercise was to see if the shorter cavity length could be maintained whilst also retaining the magnification and equivalent fresnel numbers of the extended cavity configuration. It should be noted that the output coupler, M1 (figure 3.1) could also have been modified to attempt this, however due to the high cost of modifying this element, this option was not undertaken.

A summary of the results from each of the models is presented in table 3.1. It was found that when the prescription of L1 was varied only one of the desired properties could be matched for a given prescription. Thus two models appear in the table, one to match the equivalent fresnel number and the other to match the cavity magnification.

Cavity Type	Cavity Length (m)	Lens, L2 ROC (m)	Equivalent Fresnel Number, N_{eq}	Magnification M
Original	2.50	14.05	1.73	2.02
Extended	2.96	14.05	1.63	2.11
Model 1	2.50	14.80	1.84	2.12
Model 2	2.50	13.48	1.63	1.93

Table 3.1. Cavity Modelling Results.

The existing lens is a plano-convex ZnSe element with the convex side facing the discharge. Only the radius of curvature (ROC) of the convex surface was varied. It can be seen from the table that a radius of curvature of 14.8 m is required to match the magnification whilst a radius of curvature of 13.48 m is required to match the equivalent Fresnel number. Siegmann[3.2] has shown that the optimum value of the equivalent Fresnel number for maximum transverse mode stability is (n + 0.5) for a circular mirror resonator and (n + 0.375) for a strip resonator, where n is an integer. In our case with a rectangular beam cross-section, the strip resonator condition applies. It is obvious that increasing the cavity length improves the transverse mode structure by some means other than changing the equivalent Fresnel number as this remains approximately constant for both the original and extended cavities. It is possible that the unstable transverse mode structure is due to parasitic oscillations from the electrodes. Increasing the cavity length results in an increase of the cavity diffraction losses and the elimination of the parasitic oscillations. When the ROC of the lens is changed to match the extended cavity magnification, the diffraction loss required can be obtained without the need to extend the cavity.

3.4 References

3.1) Jaenisch, H.M.; "Polarisation effects Tasks 3 and 4: LP140"; Final Report NASA Contract No. NAS8-36955; Delivery Order 33; (August 1990)

3.2) Siegmann, A.E.; "Lasers"; University Science Books; Mill Valley, CA.; Ch. 14-23 (1986)

3.3) Mathcad Software Program Version 2.5; Mathsoft Inc.; Cambridge,MA

4 LP-140 Discharge Characteristics

4.1 Introduction

The discharge circuit is an important component of the overall laser design as it can dramatically effect the efficiency of the laser. The circuit is designed to perform several functions.

4.1.1 Discharge Initiation

In order for a stable discharge to be formed the initial gas volume between the electrodes must undergo electrical breakdown. For this to occur homogeneously, preionisation electrons must be injected into the discharge gap prior to the main voltage pulse appearing across the electrodes. Normally a preionisation source driven by the discharge circuit provides these initial electrons. Following preionisation, the main voltage pulse is applied across the main electrodes to produce breakdown. Breakdown occurs through the rapid avalanching of the preionisation electrons to produce a plasma. For this process to occur successfully the main voltage pulse must have a fast risetime. The timing between the peak of the preionisation electron pulse and the initiation of the avalanching voltage pulse must be optimised to utilise as many of the preionisation electrons as possible so that a minimum number are lost to electron attachment processes. Much of this timing can be arranged to occur automatically by a suitable design of the discharge circuit.

4.1.2 Energy deposition

Once the discharge has been formed, it should be optimised to efficiently pump the upper vibrational level of the CO_2 lasing transition and other associated levels (such as the N_2 vibrational levels). It has been shown that there is an optimum electric field strength per molecule, known as the reduced electric field E/N for pumping the levels of interest. Correct matching of the discharge circuit impeadance to the discharge impeadance, together with the correct choice of voltage for the discharge circuit pulse forming network (pfn) ensures this criteria is met.

4.1.3 Pulse termination

If the circuit has been correctly designed to the above criteria, the discharge will normally extinguish itself homogeneously when the energy stored in the pfn has been deposited into the discharge. Occasionally for pulse forming reasons, a tail-biter switching technique may be used to terminate the discharge prior to the complete discharge of the pfn.

4.1.4 LP-140 Discharge circuit

The LP-140 discharge circuit is shown in figure 4.1. The circuit is duplicated for each of the eight discharge electrode pairs, with the exception of the thyratron and 880 MΩ bypass resistor which are common to all the circuits. There are essentially two discharge circuits in this circuit, the first is the main discharge circuit consisting of the 0.1 μF capacitor and the second comprises the three 22 nF capacitors. As there is an inductor in series with the 0.1 μF capacitor, this circuit will have a large time constant with respect to the 22 nF discharge circuit. When the thyratron is triggered, the 22 nF circuit provides a low energy fast risetime voltage pulse across the laser head. The pulse breaks down the gap between the grid and the pin electrodes to provide a preliminary preionising discharge. When the slower main discharge pulse arrives at the laser head, the main discharge gap is preionised and homogeneous breakdown occurs. The small 500 pF capacitor prevents energy from the slower main discharge pulse from being deposited into the preionisation discharge.

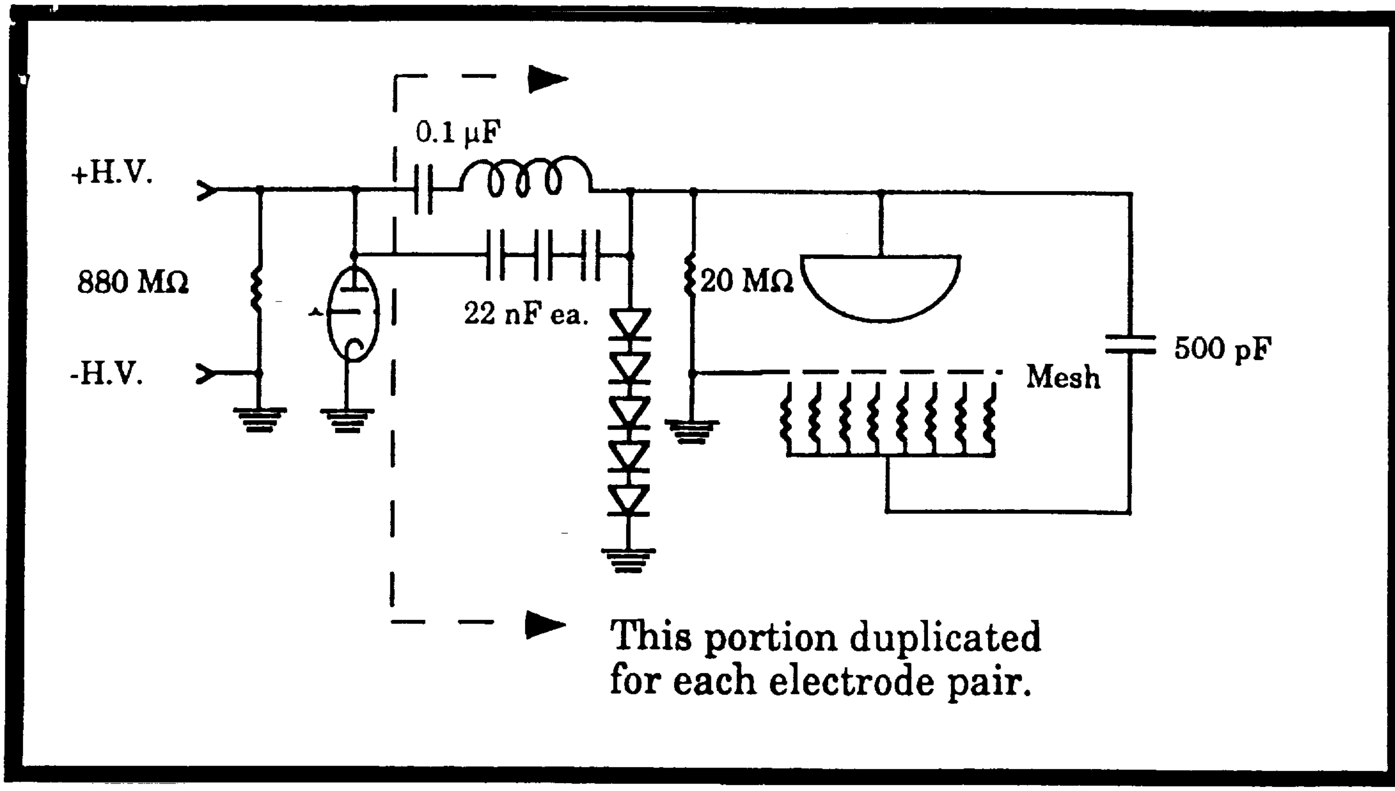

Figure 4.1. The LP-140 Discharge Circuit.

4.2 Experimental measurements

The voltage and current characteristics of the LP-140 were measured to enable the discharge to be characterised.

4.2.1 Voltage and current pulse measurements

The voltage pulse was measured using a Tektronix P6015 high voltage probe connected to a LeCroy 9450 dual 350 MHz digitising oscilloscope. The discharge current pulse was measured simultaneously using a Pearson Electronics Model 110 induction coil. After being digitised by the oscilloscope, the pulses were either ported to a plotter or to an IBM compatible computer for analysis. Figures 4.2 and 4.3 show representative voltage and current pulses from one of the electrode pairs.

4.2.2 Discharge pulse analysis

It can be seen from the voltage pulse that there is an initial sharp voltage pulse rising to -4.5 kV. This is the preionisation pulse and it is immediately followed by the main discharge pulse which rises to -5.5 kV. The voltage pulse then proceeds to ring across the discharge with an approximate average value of -4.5 kV. This ringing, allthough undesirable is not excessive. The current pulse rise is delayed with respect to the voltage rise. This is to be expected as the discharge impeadance is required to fall before a significant current flow can be obtained. The current peaks at a value of -650 A as the voltage pulse starts to fall.

Further analysis of the discharge was carried out to enable the discharge impeadance, electron concentration, electron drift velocities and energy deposition to be determined as a function of time.

The basic program Anlysvi listed in Appendix 1. was used to obtain these characteristics from the initial data files.

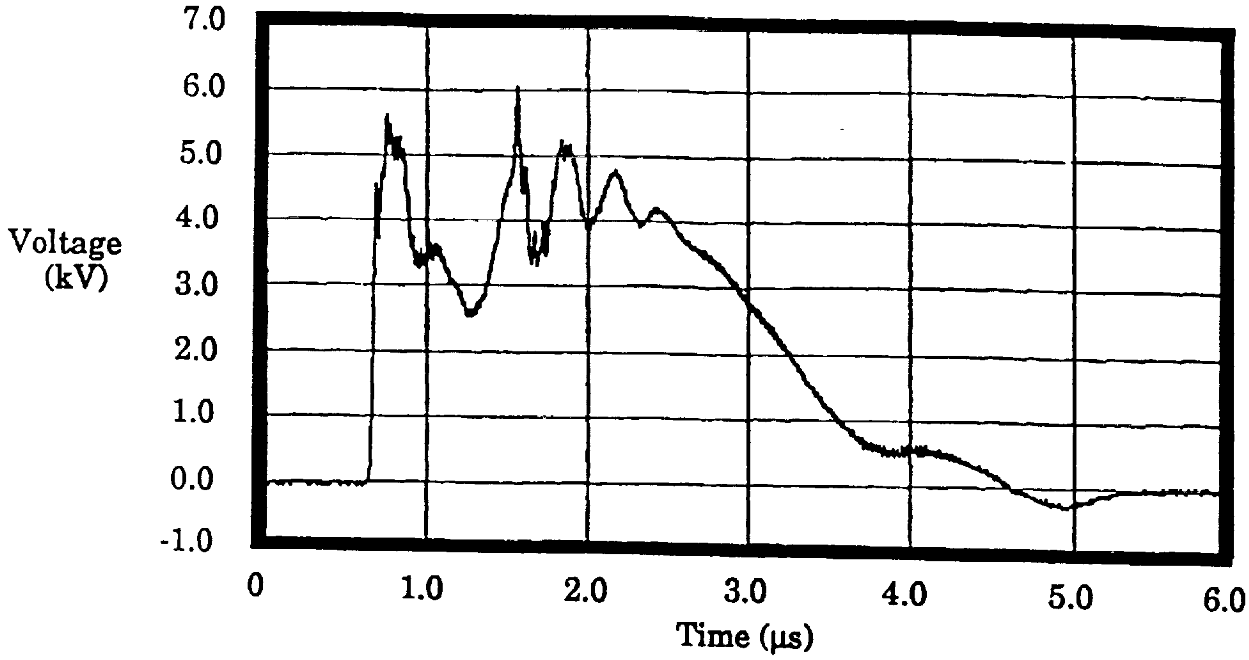

Figure 4.2. The Discharge Voltage Pulse.

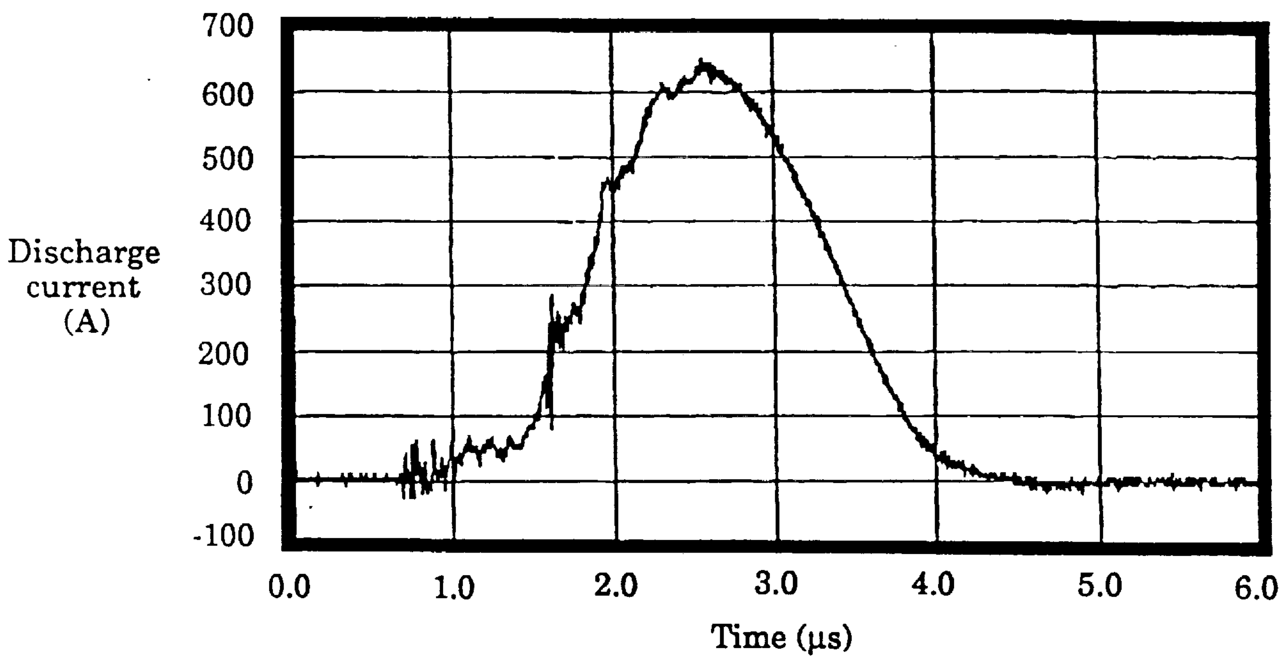

Figure 4.3. The Discharge Current Pulse.

4.2.2.1 Energy Deposition

The energy deposited into the discharge is given by:-

$$E = \int V \times I \, dt \qquad (4.1)$$

where E is the pulse energy, V and I are the voltage and current respectively and t is the time. This can be taken as:-

$$E = \sum_{n} (V \times I \times \delta t) \qquad (4.2)$$

where n is the number of digitisation intervals over the discharge pulse and δt is the sampling period. Using this enables the program to calculate the energy deposition. The energy deposition for the voltage and current pulses given earlier is shown in Figure 4.4.

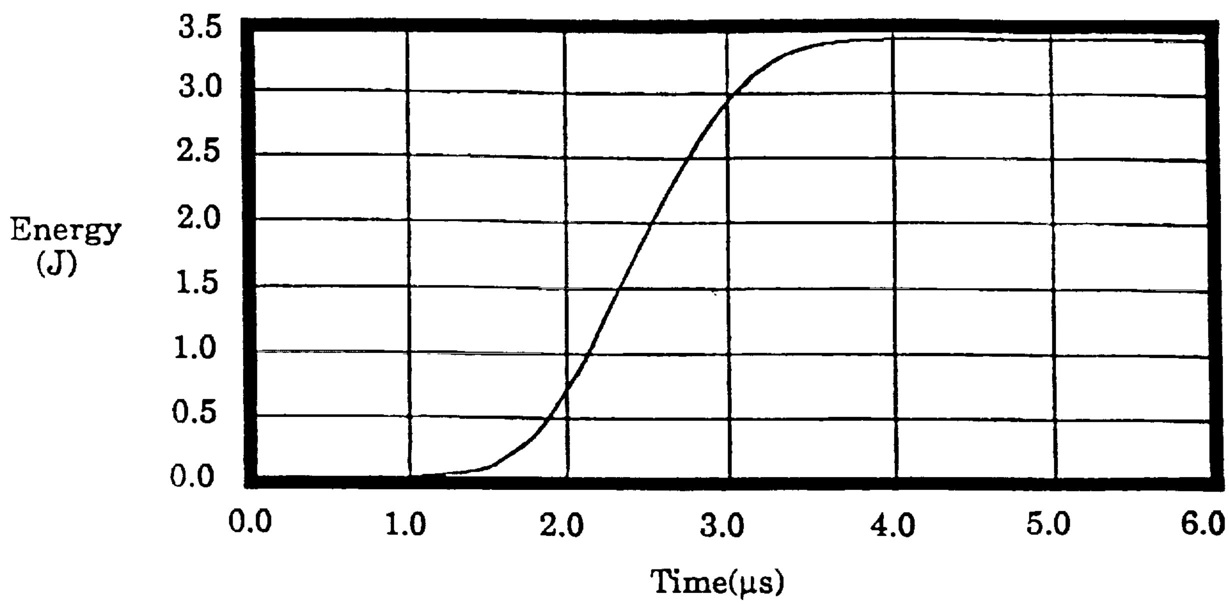

Figure 4.4. Energy Deposition in the Discharge.

It can be seen that a total of ~3.4 J is deposited into the discharge. This provides a total of 27.2 ± 3 J deposited into all eight pairs of electrodes. For a nominal optical output of 1 J this provides an electrical to optical conversion efficiency of 3.7 ± 0.2 %. This value is low compared to a potential efficiency >10 %. Only the energy deposited into the $CO_2(001)$ and the $N_2(v=1\text{-}8)$ vibrational energy levels is useful for lasing action. Lowke et al.[4.1] have shown that the optimum excitation of these vibrational levels occurs for an E/N of ~$(1\text{-}3)\times10^{-16}$ Vcm^2. The value of E/N is obtained from the voltage by:-

$$E/N = \frac{V}{d \times N} \qquad (4.3)$$

where d is the discharge electrode seperation and N is the molecular number density given by:-

$$N = \frac{P \times Vol \times NA}{R \times T} \tag{4.4}$$

where P is the total gas pressure, Vol is the discharge volume, NA is Avogadro's constant, R is the molar gas constant and T is the gas temperature. The range of E/N values during the discharge pulse is divided into intervals of 1×10^{-16} Vcm^{-2} and the energy deposited into each of the intervals is calculated (figure 4.5).

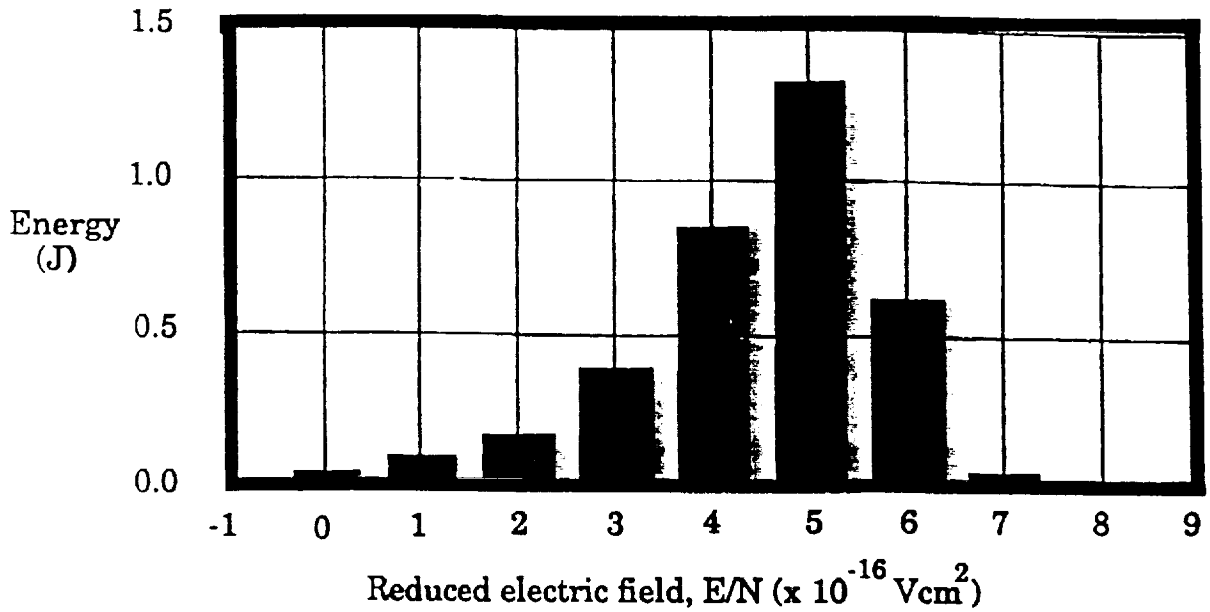

Figure 4.5. The Energy Deposition Dependence on E/N.

It can be seen that most of the energy is deposited in the $(4\text{-}6) \times 10^{-16}$ Vcm^{-2} region and this accounts for the low electrical to optical conversion efficiency obtained. To improve the efficiency, the discharge circuit impeadance should be optimised to prevent the ringing seen on the voltage pulse. Ideally the circuit impeadance should match that of the discharge. The discharge impeadance can be approximated by dividing the voltage by the current (figure 4.6). It can be seen that the discharge impeadance during the bulk of the energy deposition varies between 5 Ω and 10 Ω. This variation suggests an optimum value of ~7 Ω for the circuit impeadance. It should be noted that the discharge impeadance will vary with gas composition and optimisation of the discharge circuit should be undertaken after the final gas mixture has been decided.

4.2.3 Summary

Voltage and current pulse measurements of the LP-140 discharge were obtained and from these were derived the electrical energy deposited into the gas, the electrical to optical conversion

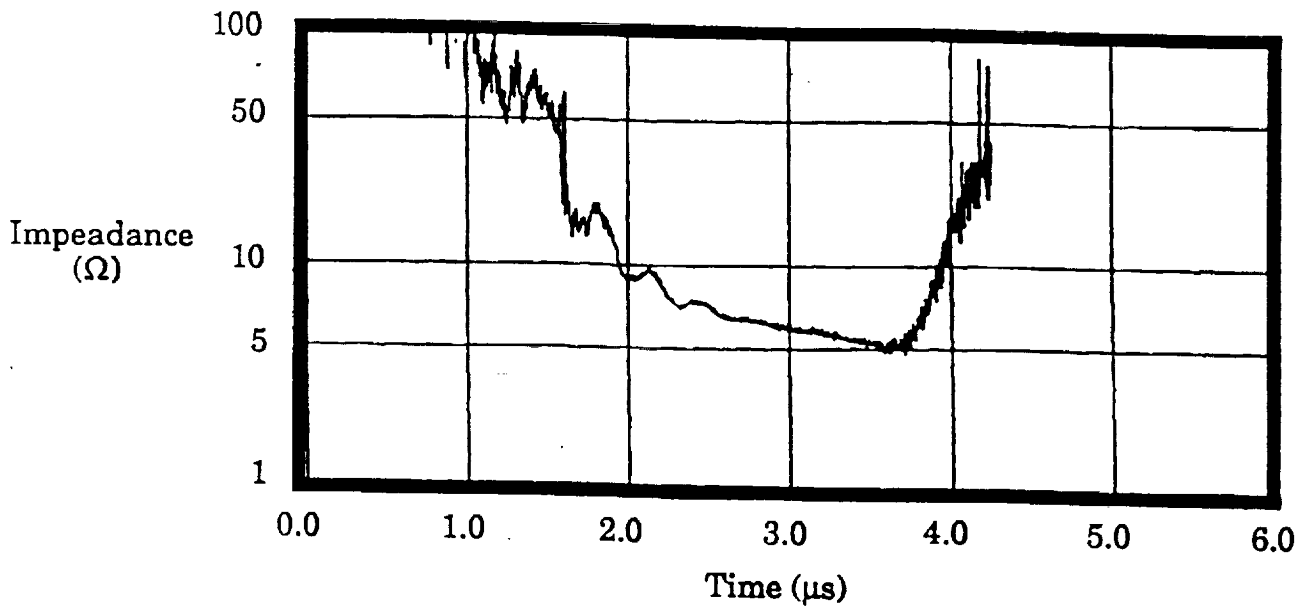

Figure 4.6. The Discharge Impeadance.

efficiency, the input energy dependence on E/N and the discharge impeadance. It was found that 3.4 J was deposited into each discharge, which had an impeadance of (5-10) Ω. A poor electrical to optical conversion efficiency of ~4 % was found to be due to ringing of the voltage pulse which resulted in the electrical energy being deposited at too high a value of E/N for efficient excitation of the relevant CO_2 and N_2 vibrational levels.

4.3 Power supply considerations

4.3.1 Introduction

This section provides an outline of assistance provided to Philip Thistlethwaite, a GSRP student who worked with the LP-140 during the later half of 1990. His task was to design a new high-voltage power supply for the LP-140.

4.3.2 Design Criteria

The following Mathcad document was provided to Philip as an initial specification requirement. A nominal design pulse rate of 20 Hz was chosen to enable the laser to be run at high pulse rates if required. The pulse energy was specified at 200 J and voltages up to 40 kV to enable higher gas pressures to be used in the laser head. This would result in shorter pulses than the (5-15) μs pulses currently obtained, together with a larger output energy. As the design of high voltage power supplies becomes more difficult with increasing voltage, the maximum voltage required was set at 20 kV but with the request that 40 kV would be desirable if he found it possible.

Power Supply Design Criteria

This determines some of the basic requirements of the high voltage power supply based on the required inputs to the laser which are;-

Maximum voltage	(V)	$V_{max} := 20000$
Maximum pulse energy	(J)	$E_{max} := 200$
Maximum pulse rate	(Hz)	$PRF := 20$
Average power	(W)	$P_{av} := PRF \cdot E_{max}$
		$P_{av} = 4 \cdot 10^{3}$

Allow a 100µS period for discharge and thyratron recovery, during which the charging unit is off, therefore the time available to pulse charge a capacitor is given by

$$t_{discharge} := 1 \cdot 10^{-4} \quad S$$

$$t_{charge} := \frac{1}{PRF} - t_{discharge}$$

$$t_{charge} = 0.0499 \quad S$$

Thus allow a 49mS charge time

$$t_{charge} := 0.049 \quad S$$

This gives an average charging current for the chosen pulse energy of

$$I_{av} := \frac{E_{max}}{V_{max} \cdot t_{charge}}$$

giving $I_{av} = 0.204$ A

The capacitor will charge exponentially where the charging current will be given by :-

$$I = I_{pk} \exp(-ct)$$

where I_{pk} is the peak charging current, c is the time constant and t is the time.

When the capacitor is fully charged the current will fall to zero, however due to the exponential decay the point at which this occurs can be said to vary, depending on how accurately the capacitor is to be charged. If we assume that we require the capacitor to be fully charged to better than 0.5% then this will give a time and time constant product of:-

$$ct := -\ln(0.005)$$

$$ct = 5.298$$

This gives for the time constant,c assuming the charging time t_{charge} above.

$$c := \frac{ct}{t_{charge}}$$

$$c = 108.129 \quad S^{-1}$$

We now need to calculate the peak charging current. The average current obtained above can be regarded as the integration of the charging current over the charging time, divided by the charging time ie

$$I_{pk} := \frac{I_{av} \cdot t_{charge}}{\int_0^{t_{charge}} \exp(-c \cdot t)\, dt}$$

$$I_{pk} = 1.087 \quad A$$

We can then plot the charging cycle

$t := 0, 0.001 .. 0.05$

$I(t) := I_{pk} \cdot \exp(-c \cdot t)$

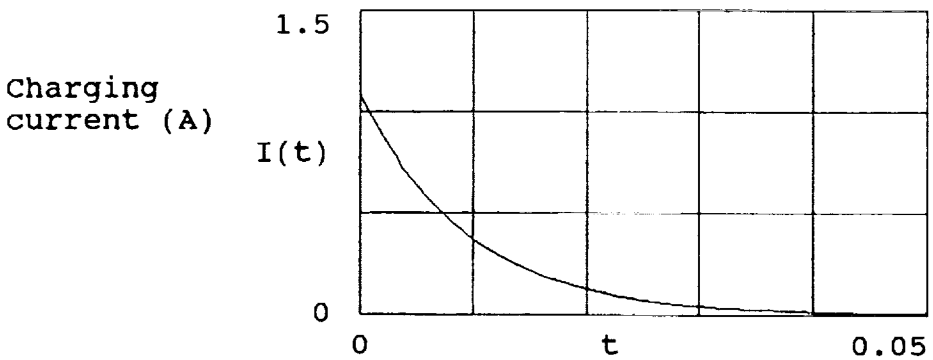

Time elapsed since start of
charging cycle (S)

4.3.3 Circuit Outline

Figure 4.7 shows a suggested circuit outline for the power supply which was provided to Philip. The input terminals on the left-hand side assume a dc source, V_{in} which charges up capacitor C1. Capacitor C2 is resonantly charged through inductor L1 to a voltage $2xV_{in}$. To ensure negligable ripple on C2, C1>C2. When C2 is fully charged thyristor, T1 is triggered to discharge C2 through the high-voltage step-up transformer, TR1. Due to the large size of T1, it requires a finite time to turn on and saturating inductor SL1 limits the current through the thyristor until turn on has been completed, at which point SL1 saturates to provide negligible resistance to the discharge pulse.

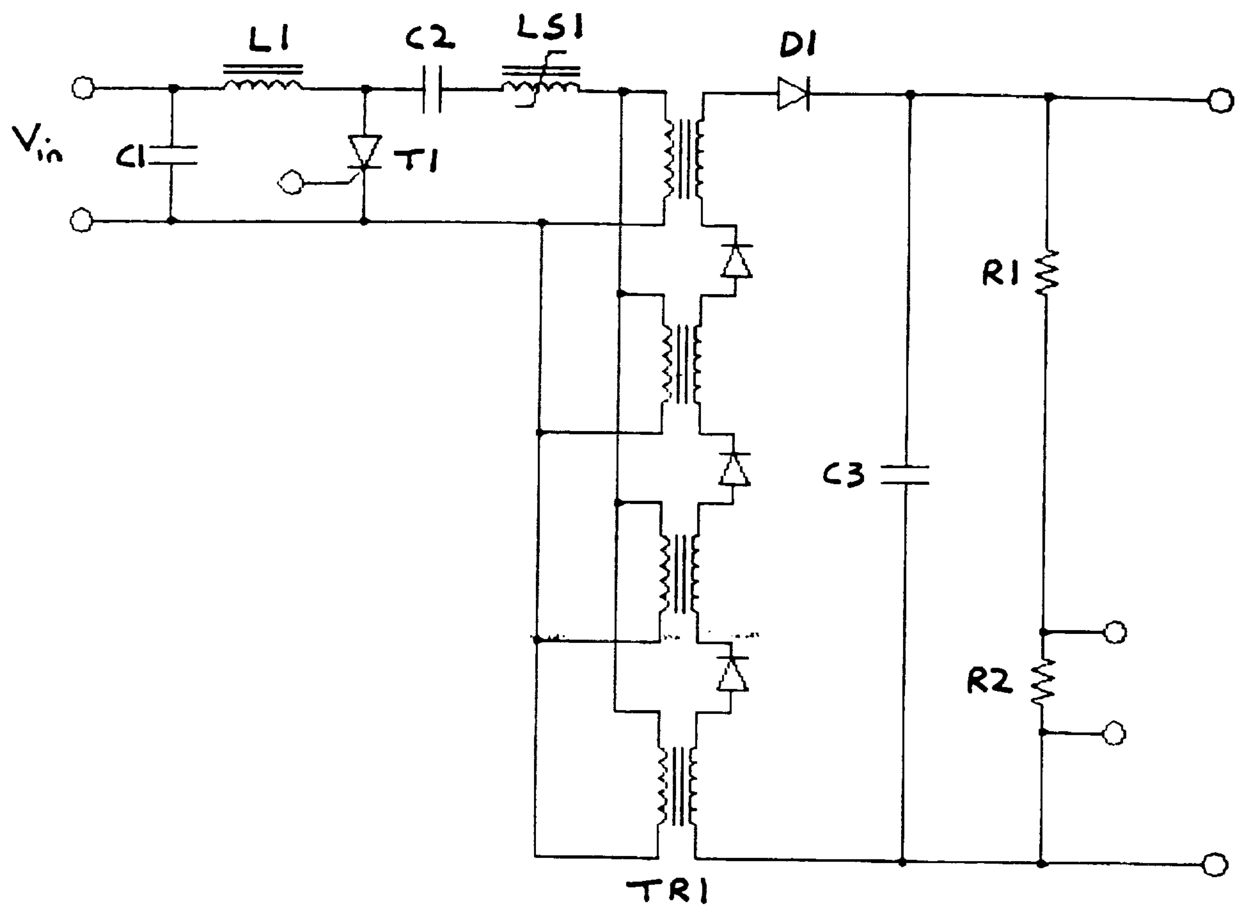

Figure 4.7. An Outline PSU Circuit.

The transformer, TR1 is shown as a distributed core transformer. This enables a large step-up ratio to be obtained whilst maintaining a low inductance for the transformer. It is possible that a single core high voltage transformer could be used. After being stepped up the pulse appears on capacitor C3. Diode, D1 prevents reverse current fluctuations from damaging the thyristor, which is vulnerable to such pulses. By choosing a suitable value of C3 and charging and discharging C2 rapidly an apparently d.c. high voltage is obtained at the output terminals. The resistive divider on the output enables the output voltage to be monitored. This monitor feeds back to the thyristor switching circuit (not shown). For a given load, varying the thyristor pulse rate will result in a variation of the output voltage.

4.3.4 Pulse Transformer Design

The Mathcad document following the references enables a design for a single core low inductance pulse transformer to be evaluated. This document was prepared following a request for a transformer design from the student. The values in the document are those for a transformer designed previously by the author[4.2]. These values were used to test the correctness of the calculations. As no specifications for the transformer were recieved from the student a final design was not completed. The theory for the design of low inductance high-voltage transformers is somewhat complex and long and the reader is therefore referred to the standard texts by Snelling[4.3,4.4] and the paper by Baker[4.5] which provide a complete review of the subject. The summary of data at the end of the document enables the optimum transformer to be chosen.

4.4 References

4.1) Lowke, J.J., A.V. Phelps & B.W. Irwin;"Predicted electron transport coefficients and operating characteristics of CO_2-N_2-He mixtures"; J. Appl. Phys.; 44; 4664 (1973)

4.2) Sylvan, A., G.D. Spiers, A. Johnstone & R.G. Harrison;"Compact high repetition rate magnetically switched transverse, electric, atmospheric CO_2 laser"; Rev. Sci. Instrum.; 61; 1821 (1990)

4.3) Snelling, E.C.;"Soft Ferrites: Properties and Applications"; Butterworths (1988)

4.4) Snelling, E.C. & A.D. Giles;"Ferrites for Inductors and Transformers"; Research Studies Press Ltd. (1983)

4.5) Baker, H.J., P.A. Ellsmore & E.C. Sille, J. Phys. E: Sci. Instrum.; 21; 218 (1988)

Pulse Transformer Design

Gary D. Spiers

Input Parameters

Peak Input Voltage	$VI_{pk} := 1000$	V
Peak Output Voltage	$VO_{pk} := 30000$	V
Voltage Ratio	$Vratio := \dfrac{VO_{pk}}{VI_{pk}}$	
Pulse Width	$\tau := 8 \cdot 10^{-6}$	s
Pulse Energy	$E := 4.32$	J

Assume pairs of 3C8 FX3845 ferrite E-cores
Assuming the cores are biased then the maximum available flux swing is $\delta B := 0.85$ T

Effective area of magnetic path	$A_e := 532 \cdot 10^{-6}$	m^2
Effective magnetic path length	$l_e := 0.147$	m
Effective magnetic volume	$V_e := 7.82 \cdot 10^{-5}$	m^3
Available winding height	$Wh := 11 \cdot 10^{-3}$	m

If we stack m cores together and vary n1, the number of turns on the primary between 1 and 7 then the condition to avoid saturation is given by:-

$$n1 := 1 \,..7$$

$$m_{n1} := \frac{VI_{pk} \cdot \tau}{\delta B \cdot A_e \cdot n1}$$

Make allowances for need to have an integral number of cores

$$m_{n1} := m_{n1} + 1 - \mathrm{mod}\left[m_{n1}, 1\right]$$

and the number of secondary turns is given by

$$n2_{n1} := n1 \cdot Vratio$$

We require an integral number of turns on the secondary

$$n2_{n1} := n2_{n1} - \mathrm{mod}\left[n2_{n1}, 1\right]$$

Now calculate the primary inductance

Relative Pulse Permeability of Core $\mu_p := 720$

Permeability of Free Space $\mu_0 := 4 \cdot \pi \cdot 10^{-7}$ H/m

$$Lp_{n1} := \frac{\mu_0 \cdot \mu_p \cdot A_e \cdot m_{n1} \cdot n1^2}{l_e} \cdot 10^6 \quad \mu H$$

Next the leakage inductance assuming a tape wound core

Thickness of material in primary winding $t_1 := 3.8 \cdot 10^{-4}$ m

Thickness of material in secondary winding $t_2 := 2.5 \cdot 10^{-5}$ m

Thickness of interwinding insulation $c := 2.4 \cdot 10^{-5}$ m

Winding Width $w := 1.9 \cdot 10^{-2}$ m

The thickness of the primary winding is thus given by:-

$$tp_{n1} := \left[t_1 \cdot n1 + c \cdot (n1 + 1)\right] \quad m$$

and the mean length per turn on the primary is given by:-

$$lp_{n1} := 2.74 \cdot 10^{-2} \cdot 2 \cdot m_{n1} + 2 \cdot 10^{-2} \cdot 2 + \pi \cdot tp_{n1} \quad m$$

Similarly for the secondary the thickness of the winding is given by:-

$$ts_{n1} := \left[t_2 \cdot n2_{n1} + c \cdot \left[n2_{n1} + 1\right]\right] \quad m$$

and the mean length per turn is:-

$$ls_{n1} := 2.74 \cdot 10^{-2} \cdot 2 \cdot m_{n1} + 2 \cdot 10^{-2} \cdot 2 + 4 \cdot tp_{n1} + \pi \cdot ts_{n1} \quad m$$

thus providing an overall mean length per turn of:-

$$l_{n1} := \frac{n1 \cdot lp_{n1} + n2_{n1} \cdot ls_{n1}}{n1 + n2_{n1}}$$

and a total winding thickness, $tw_{n1} := \left[tp_{n1} + ts_{n1} \right] \cdot 10^{3}$ mm

The leakage inductance is given by:-

$$ll_{n1} := 4 \cdot \pi \cdot 10^{-1} \cdot n1^{2} \cdot \frac{1_{n1}}{w} \cdot \left[\frac{t_{1} \cdot n1 + t_{2} \cdot n2_{n1}}{3} + c \cdot \left[n1 + n2_{n1} \right] \right] \quad \mu H$$

From the pulse energy and the input voltage we can calculate the input capacitor size

Input Capacitor $\quad C1 := \frac{2 \cdot E \cdot 10^{9}}{VI_{pk}^{2}}$ nF $\qquad C1 = 8.64\ 10^{3}$ nF

If we assume the inductance of the circuit in series with the primary and secondary coils is of the same magnitude as the leakage inductance and also assume that the capacitor on the output side of the transformer is just sufficient to hold the energy transfered across the transformer then we can calculate the transfer times for the various configurations.

Output Capacitor
Referred to primary $\quad C2 := \frac{2 \cdot E \cdot 10^{9}}{VI_{pk}^{2}}$ nF $\qquad C2 = 8.64\ 10^{3}$ nF

Series inductance $\qquad Ls_{n1} := ll_{n1}$ μH

Transfer Time

$$t_{n1} := \pi \cdot \sqrt{\left[ll_{n1} + Ls_{n1} \right] \cdot \left[\frac{C1 \cdot C2}{C1 + C2} \right] \cdot 10^{-3}} \quad \mu S$$

The actual frequency is thus given by

$$\omega_{nl} := \frac{\pi}{t_{nl} \cdot 10^{-6}} \text{ rad/s} \quad \text{and} \quad f_{nl} := \frac{1}{2 \cdot t_{nl} \cdot 10^{-6}} \text{ Hz}$$

and the actual flux swing in each core is given by

$$dB_{nl} := \frac{VI_{pk}}{nl \cdot m_{nl} \cdot A_e \cdot \omega_{nl}} \text{ T}$$

The energy losses in the transformer can be divided into two distinct sources one due to the winding and the other due to the magnetic material.

Magnetic losses
There are two sources, hysteresis loss and eddy current loss.
Hysteresis Loss

Steinmetz Exponent $n := 2.5$

Proportionality Constant $k := 2.154 \cdot 10^{-2}$
Energy loss per pulse due to hysteresis

$$Eh_{nl} := m_{nl} \cdot V_e \cdot k \cdot \left[dB_{nl}\right]^n \cdot 10^6 \text{ mJ}$$

Energy loss per pulse due to eddy currents

Resistivity of core material $\rho_f := 2 \ \Omega\text{m}$

Filling factor for core geometry $\beta := 16$

$$Ee_{nl} := \frac{\pi \cdot m_{nl}^2 \cdot A_e \cdot dB_{nl}^2 \cdot V_e}{\rho_f \cdot \beta \cdot \tau} \cdot 10^3 \text{ mJ}$$

Winding Losses

Resistivity of copper winding $\rho_c := 1.694 \cdot 10^{-8}$ Ωm

The resistances of the primary and secondary coils are thus:-

$$R1dc_{n1} := \frac{\rho_c \cdot n1 \cdot lp_{n1}}{t_1 \cdot w} \ \Omega \quad \text{and} \quad R2dc_{n1} := \frac{\rho_c \cdot n2_{n1} \cdot ls_{n1}}{t_2 \cdot w} \ \Omega$$

respectively. The peak currents in the primary and secondary can be estimated by:-

$$IP_{n1} := \frac{VI_{pk}}{\omega_{n1} \cdot \left[ll_{n1} + Ls_{n1} \right] \cdot 10^{-6}} \ \text{A}$$

and

$$IS_{n1} := \frac{VO_{pk}}{\omega_{n1} \cdot \left[ll_{n1} + Ls_{n1} \right] \cdot 10^{-6} \cdot Vratio^2} \ \text{A}$$

respectively. The energy loss per pulse in the core windings due to the d.c. resistance can then be calculated:-

$$Eres_{n1} := \left[IP_{n1}^2 \cdot R1dc_{n1} + IS_{n1}^2 \cdot R2dc_{n1} \right] \cdot t_{n1} \cdot 10^{-3} \ \text{mJ}$$

In general the a.c. resistance is higher than the d.c. resistance at high frequencies due to eddy currents in the windings. These manifest themselves as the skin effect and the proximity effect.

Skin effect

Penetration depth $$D_{n1} := 0.0655 \cdot f_{n1}^{-0.5} \quad m$$

Skin effect merit function for each coil is given by:-

$$M1_{n1} := \frac{t_1}{D_{n1}} \qquad M2_{n1} := \frac{t_2}{D_{n1}}$$

For these merit fuctions less than 2 the skin effect can be ignored.

Proximity Effect

For tape wound cores the energy loss per pulse is given by:-

$$Epe_{n1} := \frac{\pi^2 \cdot dB_{n1}^2 \cdot w}{24 \cdot \tau \cdot \rho_c} \cdot \left[n1 \cdot lp_{n1} \cdot t_1^3 + n2_{n1} \cdot ls_{n1} \cdot t_2^3 \right] \cdot 10^3 \quad mJ$$

The total energy loss is given by

$$Etot_{n1} := Eh_{n1} + Ee_{n1} + Eres_{n1} + Epe_{n1} \quad mJ$$

The results from these calculations are tabulated and summarised in graphical form on the following pages.

A summary of the variables in the following tables and their respective units are:-

n1, the number of primary turns (no units). This can be considered the primary variable, all other variables having been derived with respect to n1. In the following variable summary the n1 subscript has been dropped to reduce the amount of space required.
m, the number of core pairs required (no units).
n2, the number of secondary turns (no units).
Lp, the primary inductance (uH).
ll, the leakage inductance (uH).
t, the pulse transfer time (us).
dB, the calculated flux swing in the core (T).
IP, the peak current in the primary (A).
IS, the peak current in the secondary (A).
tw, the total winding thickness (mm).
M1, the skin effect merit fuction for the primary (no units).
M2, the skin effect merit function for the secondary (no units).
Eh, the energy loss due to hysteresis loss in the core (mJ).
Ee, the energy loss due to eddy current loss in the core (mJ).
Eres, the energy loss due to the d.c. resistance of the windings (mJ).
Epe, the energy loss in the windings due to the proximity effect (mJ).
Etot, the total energy loss in the transformer (mJ).

	m	n2	Lp	ll	t	dB	IP	IS	tw
n1	n1	n1	n1	n1	n1	n1	n1	n1	n1
1	18	30	58.9	0.08	2.6	0.08	5312.3	177.1	1.9
2	9	60	117.9	0.32	5.3	0.17	2584.1	86.1	3.8
3	6	90	176.8	0.77	8.1	0.27	1669.6	55.7	5.7
4	5	120	262	1.61	11.7	0.35	1159.9	38.7	7.5
5	4	150	327.4	2.68	15.1	0.45	897	29.9	9.4
6	3	180	353.6	3.86	18.1	0.6	748.2	24.9	11.3
7	3	210	481.3	6.28	23.1	0.66	586.4	19.5	13.2

	M1	M2	Eh	Ee	Eres	Epe	Etot
n1	n1	n1	n1	n1	n1	n1	n1
1	2.567	0.169	0.1	1.2	262.4	23.6	287.3
2	1.79	0.118	0.2	1.3	133.7	104.2	239.4
3	1.439	0.095	0.4	1.3	90.8	260.5	353
4	1.199	0.079	0.6	1.6	72.5	499.4	574.1
5	1.055	0.069	0.9	1.7	59	868.8	930.4
6	0.963	0.063	1.4	1.7	47.8	1477.9	1528.8
7	0.853	0.056	1.8	2	44.3	2075	2123.1

All graphs are a function of n1, the number of primary turns.

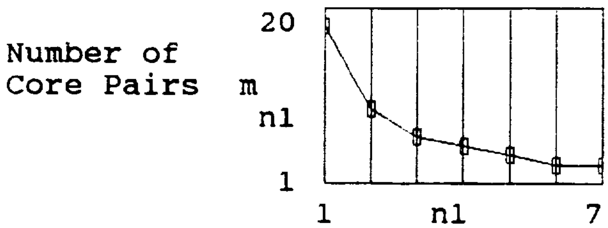

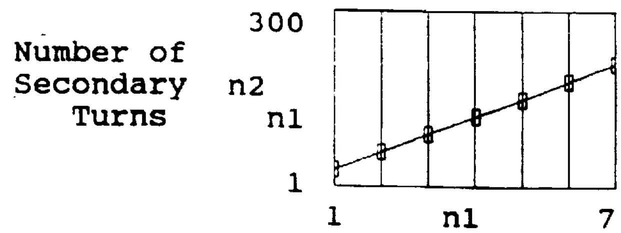

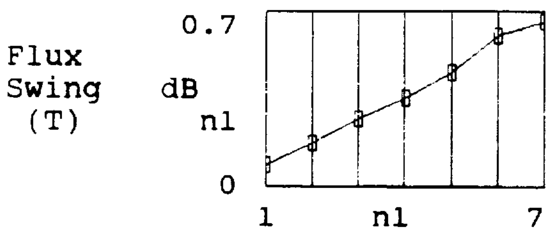

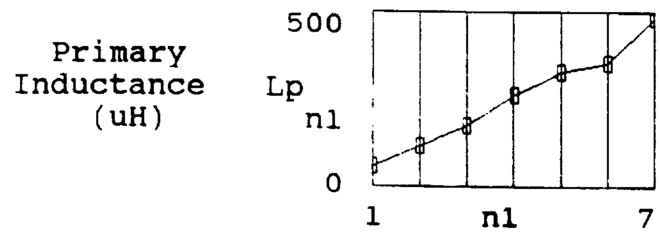

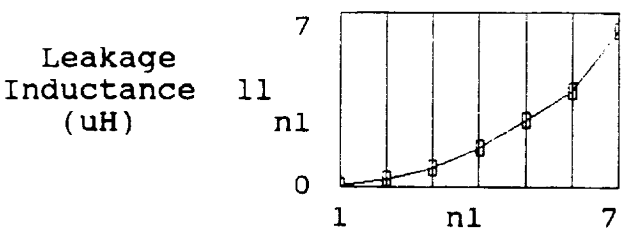

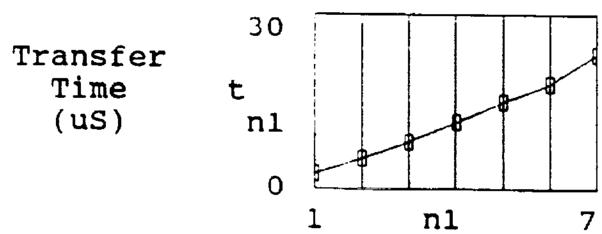

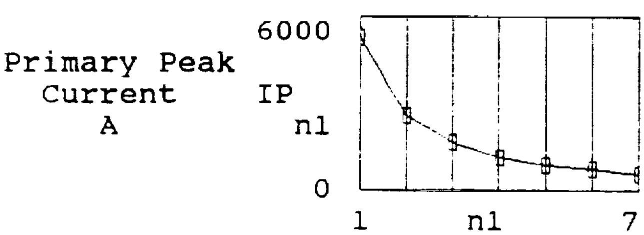

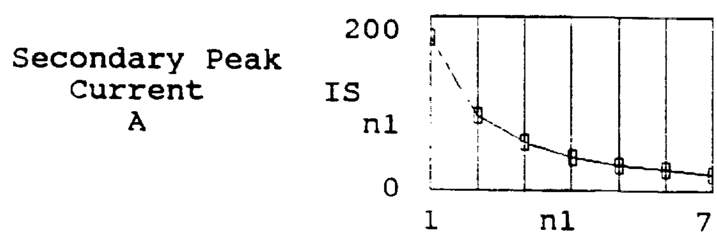

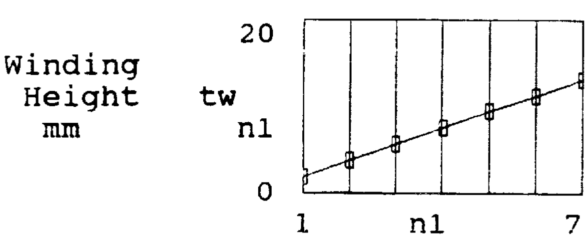

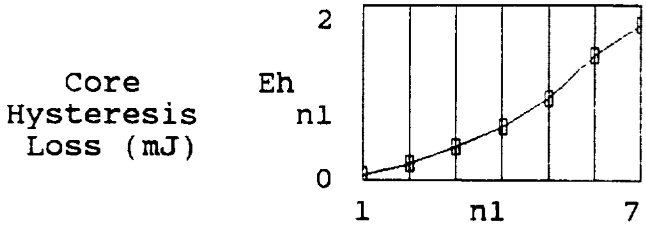
Core
Hysteresis
Loss (mJ)
Eh
nl
2
0
1
nl
7

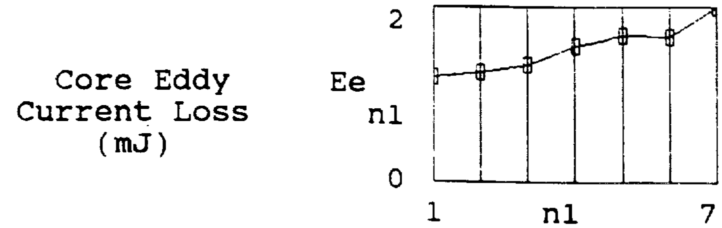
Core Eddy
Current Loss
(mJ)
Ee
nl
2
0
1
nl
7

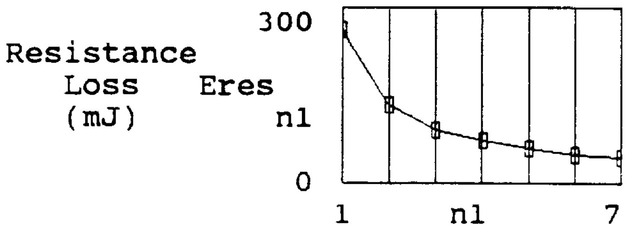
Resistance
Loss
(mJ)
Eres
nl
300
0
1
nl
7

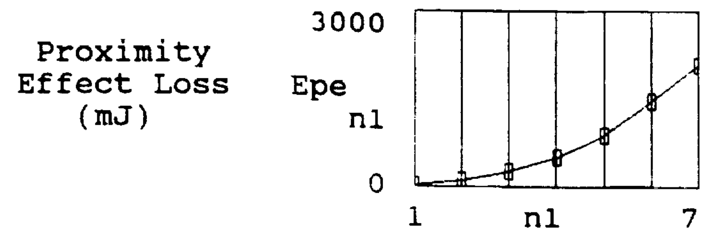
Proximity
Effect Loss
(mJ)
Epe
nl
3000
0
1
nl
7

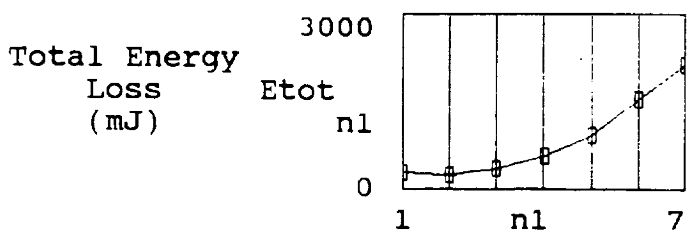
Total Energy
Loss
(mJ)
Etot
nl
3000
0
1
nl
7

5 Frequency Chirp

5.1 Introduction

There are two contributions to frequency chirp during the laser pulse, one due to the decaying electron density[5.1] in the discharge and the other due to thermal changes in the laser gas[5.2]. The thermal effect or Laser Induced Medium Perturbation (LIMP) is the main concern.

5.2 Analysis

Frequency data is collected within the laboratory on a HP time and frequency analyser and stored on an IBM compatible computer. The data is analysed using the first of the two Mathcad documents which follow. The document is self explanatory. The sample file analysed in the document is a file obtained from the LP-140. It can be seen that the total pulse length is 13 μs long with a total frequency chirp of 2.7 MHz consisting of an initial downsweep due to the decaying electron density and then an upsweep due to the LIMP contribution. Within the center of the pulse there is a 5 μs portion with a frequency chirp of 230 kHz and this has been plotted in the second window. This document has been made available to Dr. Jaenisch to enable him to analyse the chirp results from the LP-140.

5.3 Modeling

The LIMP within the laser has been modeled in Mathcad using the theory of Willetts et al.[5.2]. From the second Mathcad document we see that for a pulse length of 13 μs and a pulse energy of 1 J a frequency chirp of 2.5 MHz is obtained. As the LIMP theory is only an approximation, the degree of agreement between the measured chirp and the calculated chirp is very good, with a less than 10% difference between the two values.

5.4 References

5.1) Willetts, D.V. & M.R. Harris;"A Plasma Effect in Injection-Mode Selection of TEA CO_2 Lasers"; Appl. Phys. B; 33; 91 (1984)

5.2) Willetts, D.V. & M.R. Harris;"Scaling Laws for the Intrapulse Frequency Stability of an Injection Mode Selected TEA CO_2 Laser"; IEEE J. Quant. Electron.; QE-19; 810 (1983)

H.P. DIGITISER CHIRP DATA PLOTTING AND ANALYSIS

Gary D. Spiers

The heterodyne beat frequency obtained to measure the frequency chirp in the LP-140 is digitised by a HP digitiser and the data passed to a PC where it is stored for later use. Each file consists of 201 data points where each point consists of the point number, chirp frequency and time interval since the previous measurement respectively.
This document extracts the time and frequency information from the data file and plots two windows, the first is the total chirp over the entire pulse whilst the second is a user defined sub-window of the first. The frequency change and time duration of each window is also calculated.

$i := 0 \,..200\cdot 3 - 1$ This is the index for reading in the data.

$data_i := READ\left[chirp_{dat}\right]$ This reads the data.

$j := 0 \,..199$ Set up index for extracting required information.

The following two statements extract the chirp and time data respectively. As the original data has units of Hz and s respectively the data is also converted into kHz and μs respectively.

$$chirp_j := \frac{data_{j\cdot 3+1}}{1\cdot 10^{3}} \qquad time_j := \frac{data_{j\cdot 3+2}}{1\cdot 10^{-6}}$$

Now the two windows are set up. As the digitisation period is much longer than the pulse length, the first window is used to display the portion of relevance and the second to highlight particular areas of interest. The variables cstart, cend, sstart and send define the size of each of the windows, the units being the number of points.

$cstart := 22$ $cend := 77$ $sstart := 31$ $send := 51$

The following statements set up the index range for each window and copy the relevant data points from the original data arrays.

$k := 0 \,..(cend - cstart)$ $l := 0 \,..(send - sstart)$

$c_k := chirp_{k+cstart}$ $e_l := chirp_{l+sstart}$
$d_k := time_{k+cstart}$ $f_l := time_{l+sstart}$

The following statements find the maximum and minimum frequency in each window and calculate the total frequency chirp and time duration of each window. The frequency is also offset to provide a minimum frequency of 0 kHz to enable convenient plotting.

$minc := min(c)$ $mine := min(e)$
$maxc := max(c)$ $maxe := max(e)$

$\delta chirp1 := maxc - minc$ $\delta chirp2 := maxe - mine$

$c_k := c_k - minc$

$time1 := \sum_k d_k$

$e_l := e_l - mine$

$time2 := \sum_l f_l$

Finally plot the data and display the calculated data.

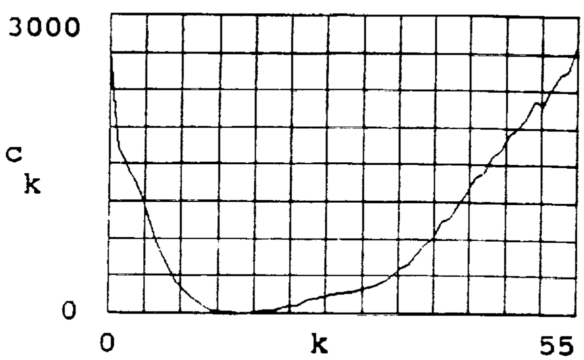

$time1 = 13$ μs

$\delta chirp1 = 2700$ kHz

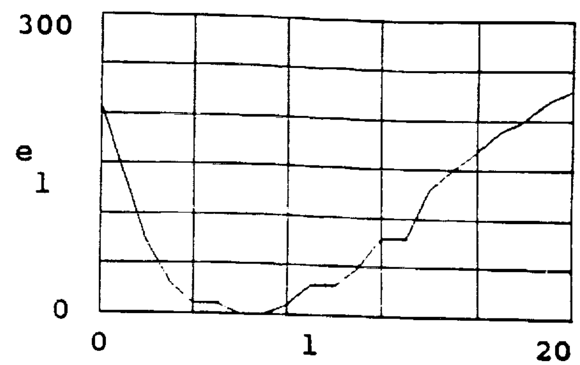

$time2 = 5$ μs

$\delta chirp2 = 230$ kHz

Laser Induced Medium Perturbation
Gary Spiers

Gladstone-Dale coefficient,	$K := 2.11 \cdot 10^{-4}$
Equivalent frequency of lower laser level, 41.9 THz for 10 μm band, 38.7 THz for 9 μm	$f0 := 41.9 \cdot 10^{12}$
Output pulse energy,(J)	$E := 1.0$
Molar gas constant,	$R := 8.314$
Mode spot radius,(M)	$\sigma := 1.25 \cdot 10^{-2}$
Cavity length,(M)	$L := 2.5$
Specific heat capacity at constant volume,	$Cv := 16.97$
Optical Pulse length,(μS)	$\tau := 13$
Time,t (μS)	$t := 0, 0.1 .. \tau$

$$f(t) := \frac{2 \cdot K \cdot f0 \cdot E \cdot R \cdot t^3}{3 \cdot \pi \cdot \sigma^4 \cdot L \cdot Cv \cdot \tau \cdot 10^{15}}$$

The factor of 10^15 accounts for the conversion of t and τ from μS to S and Hz to kHz

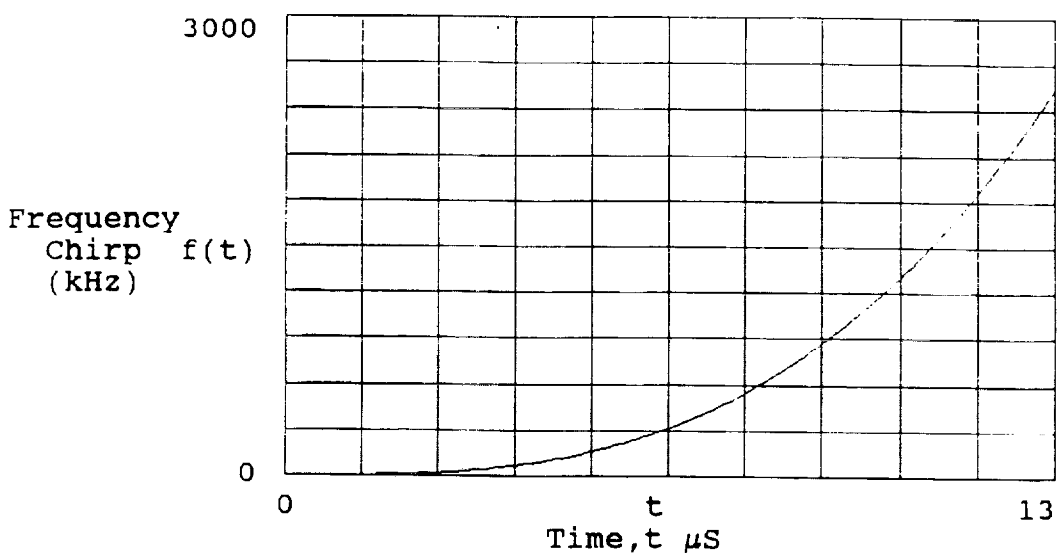

Total frequency chirp, $f(\tau) = 2545$ kHz

6 Laser Linewidths

6.1 Introduction

The laser linewidth is important in determining the likelihood of obtaining single axial mode operation. For pressures above 20 torr the CO_2 linewidth is a combination of two lineshapes. The first is due to Doppler broadening, which is the dominant mechanism at low pressure, and has a Lorentzian lineshape. The second and usually much larger contribution arises from collision broadening which has a Gaussian profile. The combined profile is known as a Voigt profile. For pressures above ~50 torr however the collision broadening is so much larger than the Doppler broadening that the Doppler can be ignored for most situations. The Mathcad document that follows calculates a Gaussian lineshape to approximate the Voigt profile. This enables a comparison between the LP-140 and the lasers proposed by the LAWS contractors to be made. For the LAWS lasers this approximation is inconsequential, however for the LP-140, which operates at a much lower pressure, there will be a slight error.

6.2 LP-140, LMSC/AVCO and GE/STI Laser Comparison

Table 6.1 lists a comparison of the results obtained for each of the lasers. LP140a is the LP-140 with a short pulse gas mixture and LP-140b with a long pulse gas mixture.

Laser	Cavity Length (m)	P (torr)	CO_2 (%)	N_2 (%)	Linewidth FWHM (MHz)	Axial Mode Sepn. (MHz)	No. modes under FWHM
LP-140a	2.38	45	52	29	343	63	5.4
LP-140b	2.38	45	13	15	291	63	4.6
LMSC/AVCO	2.20	380	25	25	2215	68	32.5
GE/STI	3.00	380	17	33	2151	50	43

Table 6.1. LP-140, LMSC/AVCO and GE/STI Laser Mode Comparison

From the table it can be seen that there is a distinct difference between the LP-140 and the LAWS lasers. This is due to the difference in operating pressures, the LAWS laser linewidths are dominated by the collision broadening. The number of axial modes under the FWHM of the linewidth indicates the likelihood of axial mode hopping, the greater the number the more likely mode hopping will occur. Thus in principle the LP-140 should easily hold a single axial mode, however due to its construction it exhibits considerable thermal drift which negates the narrow linewidth advantage. A cavity length increase of 5 μm is sufficient to change the axial mode yet perspex and aluminium, the two main components of the LP-140 construction have thermal expansion coefficients of 85 $\mu m K^{-1}$ and 23 $\mu m K^{-1}$ respectively. For a mechanical resonator length of ~1 m this implies a temperature stability of ~(0.25-0.06)K is required to keep the resonator stable.

6.3 The Mathcad Document

As mentioned previously this document only approximates a Voigt profile, however modifications are in hand to calculate the exact profile.

Laser Linewidth Calculation (LP-140)

Gary D. Spiers

This calculation normalises the gain shapes to one.

Cavity length,(m)	$L := 2.38$
Speed of light in vacuo, (m/s)	$c := 2.99792458 \cdot 10$
Wavelength of interest, (m)	$\lambda_c := 10.6 \cdot 10^{-6}$
Rotational line number	$J := 20$
Total gas pressure, (torr)	$P := 45$
Fractional CO2 concentration	$CO2 := .5193$
Fractional N2 concentration	$N2 := 0.2909$
Fractional He concentration	$He := 1 - CO2 - N2$
Gas Temperature, (K)	$T := 300$
Avogadro's number, (/mol)	$NA := 6.0221367 \cdot 10^{2}$
Boltzmann's constant , (J/K)	$k := 1.380658 \cdot 10^{-2}$
Molecular mass of CO2, (Kg/mol)	$MCO2 := 44.0098 \cdot 10^{-3}$
No. of points calculated	$imax := 400$

Doppler Broadening (FWHM)

$$\delta vd := \sqrt{\frac{8 \cdot \ln(2) \cdot k \cdot T}{\left[\frac{MCO2}{NA}\right] \cdot c^2}} \cdot \frac{c}{\lambda_c}$$

$$\delta vd = 5.289 \; 10^{7} \quad \text{Hz}$$

Collision Broadening (FWHM)

$$\delta vc := \frac{20.660 \cdot (7.520 - 0.059 \cdot J) \cdot P}{\sqrt{T}} \cdot (CO2 + 0.73 \cdot N2 + 0.64 \cdot He) \cdot 10^{6}$$

$$\delta vc = 2.903 \; 10^{8} \quad \text{Hz}$$

Total broadening (FWHM)

$$\delta vc := \delta vc + \delta vd$$

$$\delta vc = 3.432\ 10^{8} \quad \text{Hz}$$

Axial Mode Seperation

$$\delta vax := \frac{c}{2 \cdot L}$$

$$\delta vax = 6.298\ 10^{7} \quad \text{Hz}$$

$$nax := \frac{\delta vc}{\delta vax}$$

Lineshape calculation

$$i := 1, 2 \,..\, imax$$

$$v_i := \left[282813 + \frac{i}{20}\right] \cdot 10^{8}$$

$$\lambda_i := \frac{c}{v_i}$$

$$\alpha c_i := \frac{\delta vc^2}{4 \cdot \left[v_i - \left[\frac{c}{\lambda_c}\right]\right]^2 + \delta vc^2}$$

Axial mode plotting calculations

$j := 1 .. imax + 1$

$int_j := 0$

$$step := \frac{imax \cdot \delta vax}{v_{imax} - v_1}$$

$$int_i := i - mod(i, step)$$

$$\delta vc := \delta vc \cdot 10^{-6}$$

(Conversion to MHz)

$$d_i := if\left[int_i \neq int_{i+1}, 0.5, 0\right]$$

LP-140 Linewidth

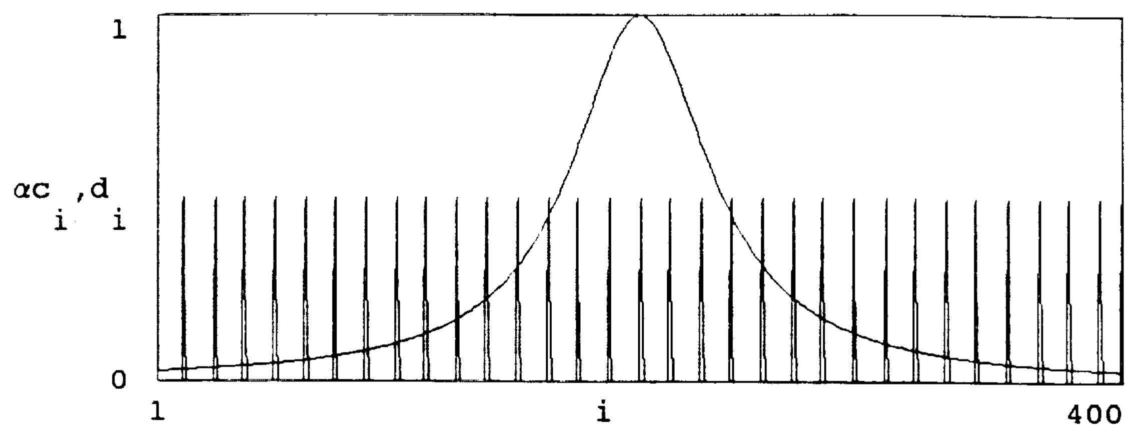

Frequency

	Minimum	Maximum
Frequency, (Hz)	$v_1 = 2.82813\ 10^{13}$	$v_{imax} = 2.82833\ 10^{13}$
Wavelength, (m)	$\lambda_{imax} = 1.05996\ 10^{-5}$	$\lambda_1 = 1.06004\ 10^{-5}$

Linewidth (FWHM), $\delta vc = 343.2$ MHz

No. of axial modes under the FWHM, $nax = 5.4$

7 Appendix (1)

```
'                          PROGRAM ANLYSVI
'
'                          Gary D. Spiers
'
'        Center for Applied Optics, University of Alabama,
'              Huntsville, Al. 35899, (205) 895 6030
'
' This program processes digitised voltage and current pulses obtained
' from the LeCroy 9450 350 MHz digitising oscilloscope. The data has been
' previously saved to disc using program LECROY, written by Phil Kromis of
' Boeing Computer Services. This program stores the data in two forms, the
' raw data direct from the digitiser (contained in the directory c:\lecroy\
' lcrdata) and decoded data (in the directory c:\lecroy\lcpdata). This
' program uses the processed data as input. The data in these processed files
' is stored as follows:-
'
' Vertical axis gain per digitisation point (Volts or Amps)
' Vertical offset (Volts or Amps)
' Timebase interval between digitisation points (s)
' Timebase offset with respect to the oscilloscope trigger pulse (s)
' Timebase value (s/div)
' (A blank line  which may eventually contain info. added at storage time)
'  "    "     "     "     "     "          "     "     "   "    "      "
'  "    "     "     "     "     "          "     "     "   "    "      "
'  "    "     "     "     "     "          "     "     "   "    "      "
'  "    "     "     "     "     "          "     "     "   "    "      "
' 1st vertical value
' .
' .
' final vertical value
' end of file
'
'
' The output files (except for the energy dependence on E/N) are stored in a
' similar format:-
'
' Time between digitisation points (s)
' Time offset from trigger point to first digitisation point (s)
' 1st calculated vertical value in appropriate units
' .
' .
' final calculated value.
' End of file.
'
'
' The energy as a function of E/N file consists of 11 values of energy, one
' for each E/N subdivision.
' START OF PROGRAM
' Dimension the filename arrays and the array for the energy as a function
' of the reduced electric field data.
```

```
DIM file1 AS STRING * 40
DIM file2 AS STRING * 40
DIM file3 AS STRING * 40
DIM file4 AS STRING * 40
DIM file5 AS STRING * 40
DIM file6 AS STRING * 40
DIM file7 AS STRING * 40
DIM file8 AS STRING * 40
DIM file9 AS STRING * 40
DIM file10 AS STRING * 40
DIM filnam AS STRING * 15
DIM ebin(1 TO 11) AS DOUBLE

' Declare the variables used in the program

DIM d1, d2, d3, d4, d5 AS SINGLE
DIM vgain, voffset, hstep, hoffset, timebas1 AS DOUBLE
DIM igain, ioffset, tstep, toffset, timebas2 AS DOUBLE
DIM vpoint, ipoint, efn, nrgstep, oldnrg, energy AS DOUBLE
DIM impead, efnval, tempry, edrift, electron AS DOUBLE
DIM count AS INTEGER

' Assign values to constants

CONST pressure = 50                    'Total gas pressure in torr
CONST temp = 100                       'Gas temperature in centigrade
CONST R = 8.315                        'Universal gas constant
CONST elecsep = 4                      'Discharge gap in cm
CONST elecwid = 4                      'Discharge width in cm
CONST e = 1.602177D-19                 'Charge on an electron

'Assign filenames for input and output of data

file1 = "c:\lecroy\lcpdata\"
file2 = "c:\lecroy\lcpdata\"
file3 = "c:\lecroy\lcpcalc\energy.dat"
file4 = "c:\lecroy\lcpcalc\impead.dat"
file5 = "c:\lecroy\lcpcalc\efn.dat"
file6 = "c:\lecroy\lcpcalc\edrift.dat"
file7 = "c:\lecroy\lcpcalc\electron.dat"
file8 = "c:\lecroy\lcpcalc\voltage.dat"
file9 = "c:\lecroy\lcpcalc\current.dat"
file10 = "c:\lecroy\lcpcalc\nrgven.dat"

'Clear the screen and obtain the names of the digitised voltage and
'current pulses to be analysed.

SCREEN 9
CLS
INPUT "Voltage filename "; filnam
file1 = LEFT$(file1, 18) + filnam
INPUT "Current filename "; filnam
file2 = LEFT$(file2, 18) + filnam


'Open up the files for input and output respectively
```

```
OPEN file1 FOR INPUT AS #1                    'Input voltage
OPEN file2 FOR INPUT AS #2                    'Input current
OPEN file3 FOR OUTPUT AS #3
OPEN file4 FOR OUTPUT AS #4
OPEN file5 FOR OUTPUT AS #5
OPEN file6 FOR OUTPUT AS #6
OPEN file7 FOR OUTPUT AS #7
OPEN file8 FOR OUTPUT AS #8
OPEN file9 FOR OUTPUT AS #9

' Read in the voltage gain and offset, digitisation time interval,pre/post
'trigger delay interval and oscilloscope timebase setting for the voltage
'pulse followed by five blanks to seperate the header from the data

INPUT #1, vgain, voffset, hstep, hoffset, timebas1
INPUT #1, d1, d2, d3, d4, d5

'Repeat the above procedure for the current pulse to obtain current gain and
'offset, digitisation time interval, pre/post trigger delay interval and
'oscilloscope timebase setting for the current pulse.

INPUT #2, igain, ioffset, tstep, toffset, timebas2
INPUT #1, d1, d2, d3, d4, d5

' As the two pulses were digitised simultaneously the digitisation intervals
' and offsets should be the same. If there is a difference this implies an
' error in the data or possible incorrect pairing of the voltage and
' current data files. If they are not the same then issue a warning and stop
'the program.

IF toffset <> hoffset OR hstep <> tstep THEN
 PRINT "Voltage and Current files are incompatible !"
 CLOSE
 STOP
END IF

' As all of the output files except the energy deposition as a function of the
' reduced electric field are time dependent, write the digitisation interval
' and trigger offset to the top of each file (except Energy as fn. of E/N).


WRITE #3, tstep
WRITE #3, toffset
WRITE #4, tstep
WRITE #4, toffset
WRITE #5, tstep
WRITE #5, toffset
WRITE #6, tstep
WRITE #6, toffset
WRITE #7, tstep
WRITE #7, toffset
WRITE #8, tstep
WRITE #8, toffset
WRITE #9, tstep
WRITE #9, toffset
```

```
' Set up a loop with counter to incrementally read in the data points and
' calculate the required information.

count = 0
CLS
LOCATE 10, 28
PRINT "Processing point no."

DO
 LOCATE 10, 49
 PRINT count
 INPUT #1, vpoint
 INPUT #2, ipoint

'Firstly take the raw data points and convert them to units of volts and amps

 vpoint = -(vpoint * vgain - voffset)
 ipoint = (ipoint * igain - ioffset)

' Then store these voltage and current values in their output data files so
' that they may be plotted

 WRITE #8, vpoint
 WRITE #9, ipoint

' Now calculate the reduced electric field, E/N and store the value

 efn = ((273.15 + temp) * R * vpoint) / (80.2853 * 10 ^ 18 * pressure * elecsep)
 WRITE #5, efn

' Multiplying the voltage by the current and timestep provides the input
' energy for each discrete digitisation interval. This energy per step is
' stored in an array for use later to evaluate the energy as a fn. of E/N.
' The individual packets of energy are summed to provide the total energy
' input into the discharge and stored to file. this provides a record of
' the time evolution of the energy into the discharge.

 nrgstp = vpoint * ipoint * tstep
 IF count = 0 THEN
  energy = nrgstp
  ELSE
  energy = oldnrg + nrgstp
 END IF
 oldnrg = energy
 WRITE #3, energy

' The discharge impeadance at each digitisation point is found by dividing
' the voltage by the current. However in the initial and final parts of the
' digitisation both the current pulse is zero and the division results in
' an infinite impeadance which creates an overflow error. Additionally the
' current fluctuates by +/- 1 digitisation point (an artifact of the
' digitisation process) about the zero level to provide spurious values
' of the impeadance which are artificial and due entirely to the digitisation.
' To eliminate this traps for the magnitude of the discharge current <0.1 A
' (c.f. peak values of ~500+ A) have been set and when this occurs the
' impeadance is set to 200 ohms which is sufficiently large with respect to
```

```
' the actual impeadance after breakdown has occured to be representative of
' the actual infinite value prior to breakdown. The resulting impeadance
' value is saved to file.

 IF ABS(ipoint) < .1 THEN
  impead = 200
  ELSE
  impead = vpoint / ipoint
 END IF
 IF impead <= 0 THEN impead = 200
 WRITE #4, impead

' This routine subdivides the input energy as a function of the E/N value.
' The E/N is divided into 10 boxes, each representing a step of 1x10^(-16)
' Vcm^(3) in the range (0->10)x10^(-16) Vcm^(3) plus an eleventh box for
' all values greater than 10x10^(-16) Vcm(3). As only the final total for
' each box is required no saving to file is done at this point.

 efnval = ABS(efn) * 10 ^ 16
 IF efnval < 10 THEN
  ebin(INT(efnval + 1)) = ebin(INT(efnval + 1)) + nrgstp
 ELSE
  ebin(11) = ebin(11) + nrgstp
 END IF

' The following calculates the electron drift velocity and electron density
' in the discharge. The electron density depends on the electron drift which
' depends in a non-linear fashion on the reduced electric field E/N. The
' paper "Predicted electron transport coefficients and operating
' characteristics of CO2-N2-He laser mixtures" by J.J. Lowke, A.V. Phelps and
' B.W. Irwin in J. Appl. Phys., 44, 10, 4664-4671, (1973) calculated this
' dependence for several gas mixtures. From the results presented we can see
' that :-
'
'                    log(drift velocity) = b + k.log(E/N)
'
' approximately. Allthough crude this approximation enables an order of
' magnitude estimate of the electron drift velocity to be made simply. This
' technique has been used within this program with b=17.044 and k=0.658.
'
' A trap is used to prevent a value of zero volts resulting in an overflow
' error. Finally the calculated data is saved to file.

 IF vpoint <> 0 THEN
  tempry = LOG(ABS(efn)) / LOG(10)
  edrift = 10 ^ (17.044 + .658 * tempry)
  electron = (ipoint / (elecsep * elecwid * e * edrift))
 ELSE
  electron = 1
  edrift = 1
  END IF
 WRITE #6, edrift
 WRITE #7, electron
```

```
' Increment the loop counter and if either of the input data files is
' empty then leave the loop and close all the files.

 count = count + 1
LOOP UNTIL EOF(1) OR EOF(2)
CLOSE

' Finally the output energy dependence on E/N data must be written to file
' and then end the program.

OPEN file10 FOR OUTPUT AS #10
count = 1

DO
 WRITE #10, ebin(count)
 count = count + 1
LOOP UNTIL count = 12

CLOSE
CLS
LOCATE 10, 28
PRINT "Analysis successfully completed."
END
```

8 **Appendix (2)**

Idealised Laser Mode Profiles

This program calculates the Rayleigh range for a given Gaussian beam together with the spot size and mode profile at any given location. The profile calculated is the idealised rectangular mode profile of the beam at the chosen location for values of l and m, the TEM indices, up to 3. Firstly select the initial parameters:-

Minimum spot size

$$w_0 := 3 \cdot 10^{-3}$$

Wavelength

$$\lambda := 10.6 \cdot 10^{-6}$$

Refractive Index

$$n := 1$$

Calculate the Rayleigh range at the beam waist, given by:-

$$z_R := \pi \cdot w_0^2 \cdot \frac{n}{\lambda} \qquad z_R = 2.667$$

Define the beam waist location as position z=0, then chose a position for the calculation of the spot size and mode profile:-

$$z_0 := 0 \qquad z := 5$$

Calculate the spot size at the chosen location using:-

$$w := \sqrt{w_0^2 \cdot \left[1 + \frac{z^2}{z_R^2}\right]} \qquad w = 0.006$$

Then calculate the radius of curvature of the beam at the chosen location using:-

$$R := z \cdot \left[1 + \frac{z_0^2}{z^2}\right] \qquad R = 5$$

Now start on the mode profile by chosing values for l and m, the mode indices, and the electric field, E. The mode is calculated using a 50x50 array of points.

$$l := 2 \qquad m := 2 \qquad E_0 := 1 \qquad \begin{matrix} q := 0 \,..50 \\ v := 0 \,..50 \end{matrix}$$

Next calculate the relevant x and y Hermite polynomials for the chosen mode profile:-

$$H_x(x) := \mathrm{if}\Big[l \approx 0, 1, \mathrm{if}\Big[l \approx 1, \Big[2\cdot\sqrt{2}\cdot\frac{x}{w}\Big], \mathrm{if}\Big[l \approx 2, \Big[4\cdot\Big[\sqrt{2}\cdot\frac{x}{w}\Big]^2 - 2\Big], \mathrm{if}\Big[l \approx 3, \Big[8\cdot$$

$$H_y(y) := \mathrm{if}\Big[m \approx 0, 1, \mathrm{if}\Big[m \approx 1, \Big[2\cdot\sqrt{2}\cdot\frac{y}{w}\Big], \mathrm{if}\Big[m \approx 2, \Big[4\cdot\Big[\sqrt{2}\cdot\frac{y}{w}\Big]^2 - 2\Big], \mathrm{if}\Big[m \approx 3, \Big[8\cdot$$

Finally calculate the intensity mode profile:-

$$I(x,y) := \left[E_0 \cdot \frac{w_0}{w} \cdot H_x(x) \cdot H_y(y) \cdot \exp\left[\frac{-\left[x^2 + y^2\right]}{w^2}\right]\right]^2$$

The following variables are associated with scaling the grid size to cover the chosen spot size, whilst M is a dummy array required by the surface plotting routines.

$$x_q := \frac{q\cdot 4\cdot w}{50} - 2\cdot w \qquad y_v := \frac{v\cdot 4\cdot w}{50} - 2\cdot w \qquad M_{q,v} := I\left[x_q, y_v\right]$$

$$\left.\left.\left.\left.\left.\sqrt{2}\cdot\frac{x}{w}\right]^{3} - 12\cdot\sqrt{2}\cdot\frac{x}{w}\right],0\right]\right]\right]\right]$$

$$\left.\left.\left.\left.\left.\sqrt{2}\cdot\frac{y}{w}\right]^{3} - 12\cdot\sqrt{2}\cdot\frac{y}{w}\right],0\right]\right]\right]\right]$$

The mode profile

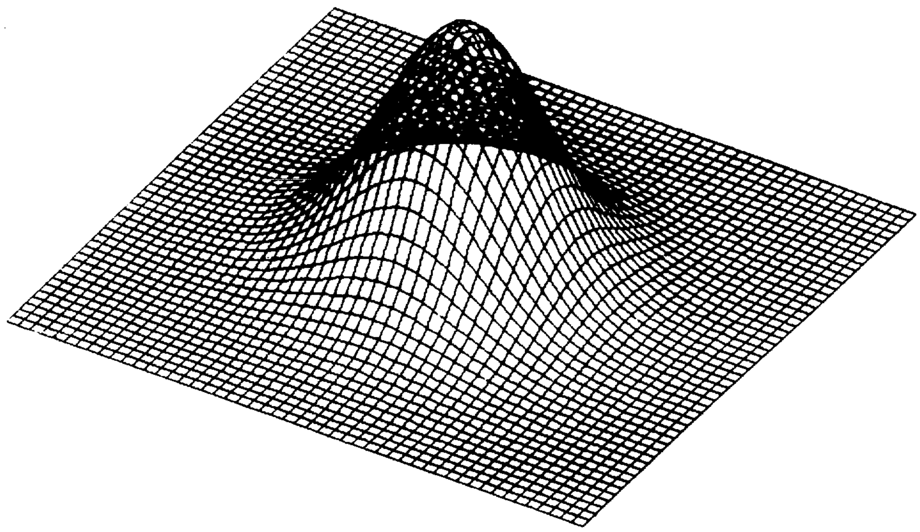

l = 0 m = 0

M

The mode profile

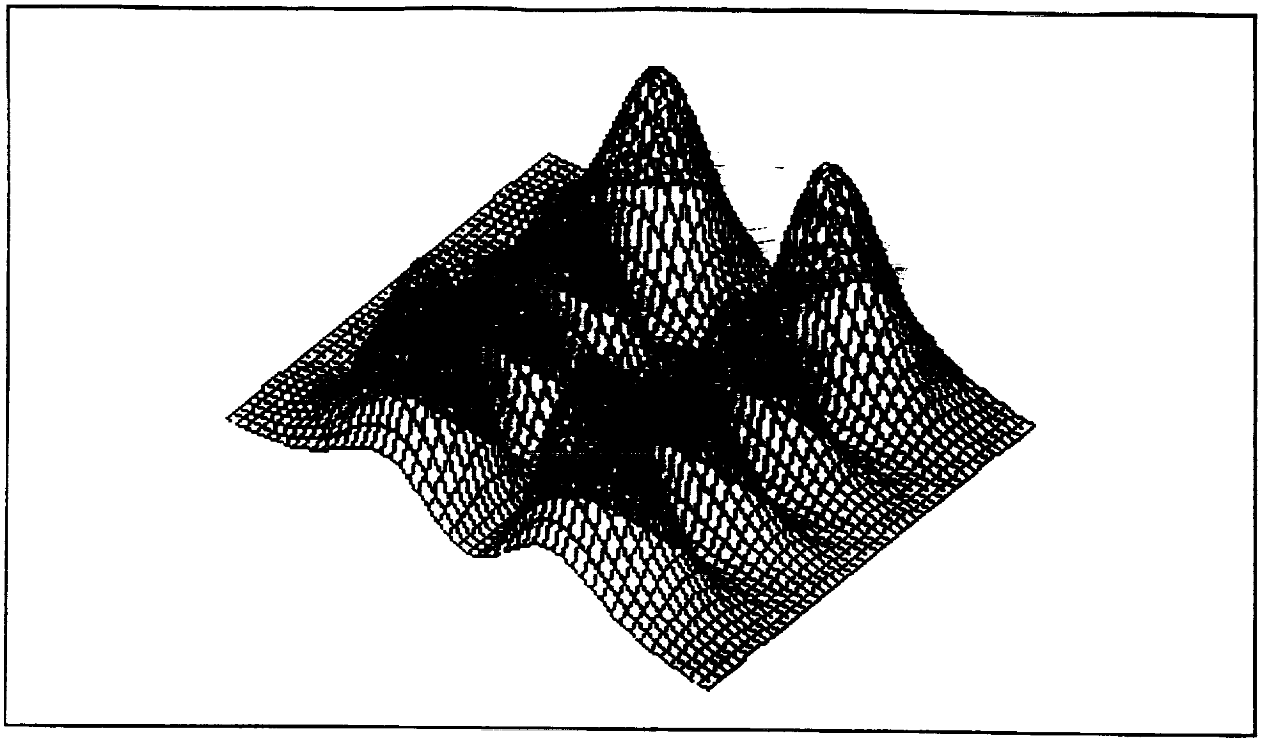

M

Transverse mode profile indices l = 3 m = 1

Modifications to the LP-140 Pulsed CO_2 Laser for Lidar Use

Holger M. Jaenisch and Gary D. Spiers
Center for Applied Optics
University of Alabama in Huntsville
Huntsville, Alabama 35899

ABSTRACT

The Pulse Systems Inc. Model LP-140 is a commercial pulsed CO_2 laser designed for marking and engraving. It is available with pulse energies in excess of 1 joule and repetition rates up to 7 Hz, thus making it a potential candidate for lidar applications. We document the characteristics of the LP-140 performance including power, temporal and spatial mode stability, chirp, and long term operational characteristics. The laser can be made to function as a coherent lidar only if modified to improve its inherent characteristics. This paper addresses work in progress on the following modifications and their effect on performance: gas flow, optical resonator configuration and discharge supply modifications.

INTRODUCTION

The LP-140 is a transversely excited pulsed discharge device based on a sympathetic discharge[1]. The system is produced and marketed commercially for applications such as engraving. The LP-140 is designed and built to the Pulse Systems Inc. (PSI) specifications[2] listed below.

- DIMENSIONS: 0.35 x 0.35 x 1.2 m^3 (this dimension includes all optical components)
- ENERGY PER PULSE: 3 J. (multi-mode with no frequency discrimination)
- GAS CONSUMPTION: 0.3 Standard Cubic Feet Per Hour (0.14 l/min)
- GAS MIX: 20% CO_2; 15% N_2; 65% He
- INPUT POWER: 115V, 50-60 Hz, @ 5 amps
- MAXIMUM PULSE RATE: 8 Hz (Higher repetition rates available but at lower pulse energies)
- PRESSURE: 40 torr
- PULSE WIDTHS: 35 μs FWHM (100 ns to 200 μs available on special order)

Our goal was to modify the LP-140 to meet the criteria outlined below.

- Minimum overall size and compactness
- Energy of 1 J per pulse
- Maximum pulse length of 5 μs
- Stable single mode operation
- Interpulse frequency stability of < 1 MHz
- Intrapulse frequency stability of < 0.2 MHz
- Maximum pulse length of 5 μs
- Maximum repetition rate of 10 Hz

These requirements were derived from the requirements of the laser systems proposed for LAWS[3] (Laser Atmospheric Wind Sounder). The LP-140 was never considered a contender for this program, however the relatively low cost, and simple, rugged design make it an attractive choice for small scale atmospheric studies if the laser performance can be improved. The LP-140 can also be used as a testbed for LAWS concepts.

LASER DESCRIPTION

The laser secured for this investigation differed from the standard commercial models on several key parameters. The active volume was extended from the ≈1.7 L of the standard design to ≈2.2 L. The standard gas mixture of CO_2:N_2:CO:He, 18:15:2:65 which produces long pulses was modified to produce short pulses (< 10μs). The new mixture was designed by PSI using a Boltzmann distribution code[4] and proprietary laser model[5]. The new mixture consists of CO_2:N_2:CO:He, in the proportions

15.29:17.33:1.99:65.39. The gas pressure is measured using a Wallace & Tiernan model FA160 gauge and the laser is operated in the 30–50 torr pressure range.

The standard LP-140 is configured for high power multi-mode operation. Our application requires mode discrimination, therefore the optical cavity design was changed to a hybrid, positive branch half-symmetric configuration using a Burleigh Instruments Model I-1000 reflection grating mounted at the Littrow angle to enable single longitudinal mode operation. The grating was also supplied with a Burleigh Instruments Model TS-100 translation stage, Model PZL-M Micrometer mount, Model PZL-015-00 15 μm PZL pusher, and a Model PZ-150-1 Amp/Driver-150 for feedback control and cavity tuning.

As presented in reference 2, each of the two gain arms has an effective volume of 4 x 4 x 70 cm^3, comprising of four equal discharge volumes, with an unsaturated gain of 0.031 cm^{-1} and a saturation intensity of 0.017 J cm^{-2}.

The standard gas flow plumbing was engineered by PSI to enhance operational lifetime. The commercial housing was maintained, but modified to allow the addition of the grating externally to the housing. The mechanical resonator structure was of a cast aluminum single piece construction.

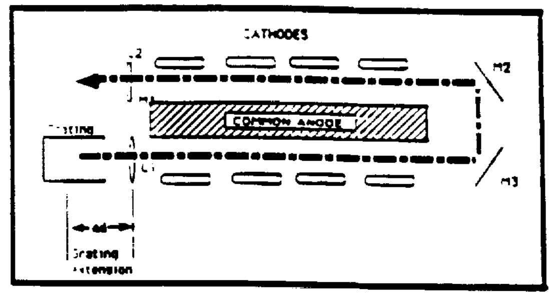

Figure 1: Optical layout of LP-140.

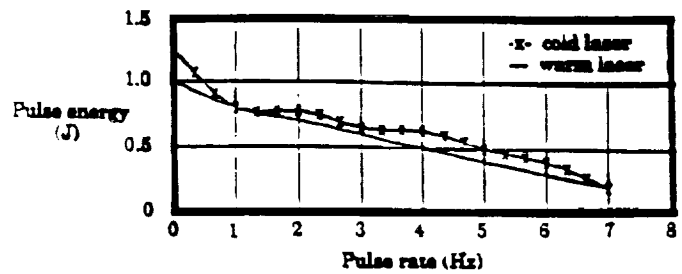

Figure 2: Pulse energy dependence upon pulse rate and laser temperature.

OPTICAL DESCRIPTION

Our LP-140 folded optical cavity consists of a 6.35 cm diameter x 0.63 cm edge thickness meniscus ZnSe output coupler with a 5m radius of curvature on both surfaces (Figure 1). The A.R. coated convex side faces the discharge, in the center of which a square gold mirror had been flashed on with an area of 4 cm^2. Two rectangular gold flat mirrors fold the optical path into the second arm of the optical cavity. Each is supported by a simple three-point mount. Finally the laser-tube cavity is sealed with a 10 m focal length, 6.35 cm diameter x 0.63 cm edge thickness A.R./A.R. plano-convex lens, with the convex side facing the discharge. The optical cavity is completed by the grating placed $\approx$ 10 cm beyond the final lens element. The optical cavity length is 238 cm. Since the 4 x 4 cm^2 discharge region is square all optical elements are underfilled. The actual beam dimensions are (center obscured) 4 x 4 cm^2.

INITIAL CHARACTERIZATION

Pulse Energy

The initial pulse energy for the system was measured as approximately 1 joule per pulse at 1 Hz. The pulse energy stability was poor and varied not only from shot to shot but decreased to below a joule after only a few minutes of operation. As the repetition rate was increased the average pulse power decreased as seen in Fig. 2. During the test it was found that a minimum of 40 minutes was required for the operational system to reach thermal equilibrium and maximum stability. Also shown on the same figure is a similar result taken after the laser had reached thermal equilibrium. It can be seen that the output energy is consistently lower than immediately after startup.

In the cool system the power varied by 10% from shot to shot, after the laser had warmed up this dropped to 5%.

Temporal Profile

The temporal profile was measured using a PSI fast response pyroelectric detector, Model # UF-1 with a responsivity of 10^{-7} V/W. To prevent detector damage the beam was attenuated before being focussed onto the detector.

Figure 3 is an example of the initial temporal profile observed during the baseline characterization. It can be seen that there is significant mode beating during the 5 μs pulse duration.

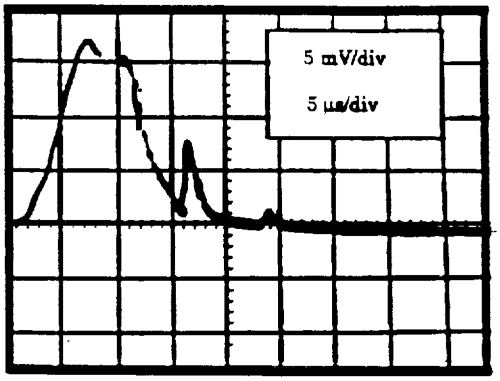

Figure 3: Pulse temporal profile prior to modification.

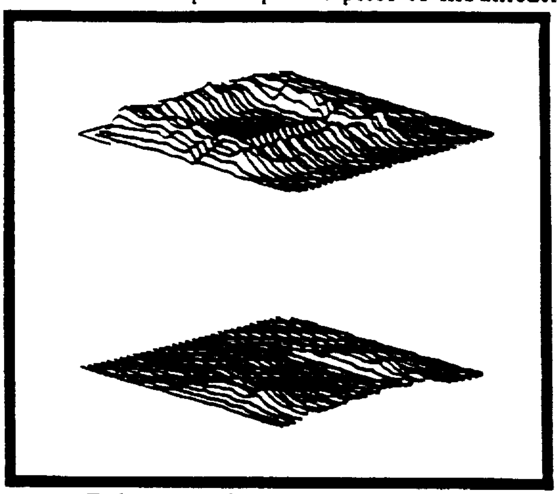

Figure 4: Pulse spatial profile prior to modification.

Spatial Profile

The spatial profile was measured using a Spiricon beam profiler and the laser transverse mode pattern was found to be highly unstable with a large degree of beam pointing instability. Local hot spots in the beam distribution would vary on a shot to shot basis indicating possible transverse mode hopping. Figure 4 shows two representative records.

Frequency Chirp

The intrapulse frequency chirp was measured by feeding the laser output into the existing Marshall Lidar[6]. The data was collected on the 10P20 line. Due to transverse mode instabilities indicated above the frequency chirp was considerable (≈8 MHz) and varied inconsistently from shot to shot.

SYSTEM MODIFICATIONS

Gas Flow

The degradation in output energy with both increased

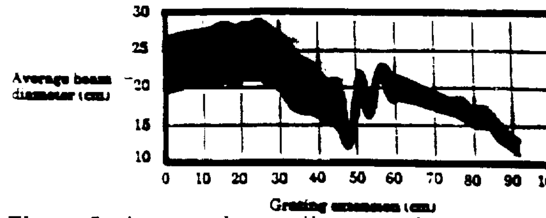

Figure 5: Average beam diameter dependence upon grating extension.

pulse rate and number of pulses tends to indicate insufficient gas flow through the laser. This results in pressure, thermal, and possible dissociation mechanisms in the gas leading to the reduced output. During operation, the needle on the pressure gauge momentarily rises by as much as 10 torr. This is indicative of the pressure wave which exists inside the cavity during the laser discharge.

Inspection of the laser head showed that the gas in and out flow were limited by the orifice size of the flow tubing. The standard LP-140 laser flows gas through the discharge at a trickle rate of 0.5 L/min. The gas flow was modified by increasing the diameter of the input and output lines and reversing the direction of flow in the laser head. This enabled the flow rate to be increased to 2.5 L/min.

Cavity Length

The cavity was lengthened by increasing the spacing between the grating and the lens, L1 (Fig. 1). This enabled a more stable operation point to be obtained. Additionally the increased path length reduces spurious off-axis modes. The cavity was extended in 2.54 cm increments. Previously, the grating would have to be adjusted every two to three shots to maintain a uniform laser output. For an extension of 53±5 cm the distribution became very uniform and stable. The optimum beam stability (Fig. 5) and mode pattern points did not coincide. The energy increased to approximately 1.25 joules (Fig. 6) for an extension of 51 cm but there was very slight mode instability characterized by the occasional appearance and disappearance of a mode hot-spot.

At 54 cm extension the beam pointing instability was minimized. At 56 cm the energy decreased to 1.15 joules and the mode distribution was at its most stable point. The output quickly became chaotic as the cavity extension decreased below 45 cm. There was also an accompanying energy drop to 0.75 joules for extensions below 25 cm. As the cavity spacing was further decreased, the energy once again increased. For extensions above 58 cm the power dropped off linearly. Mode and pointing instability never set in for cavity extensions out to 90 cm. Although stable, the output energy distribution collapsed to fill only a single corner of the entire possible output pattern. This corner remained very stable in distribution but fluc-

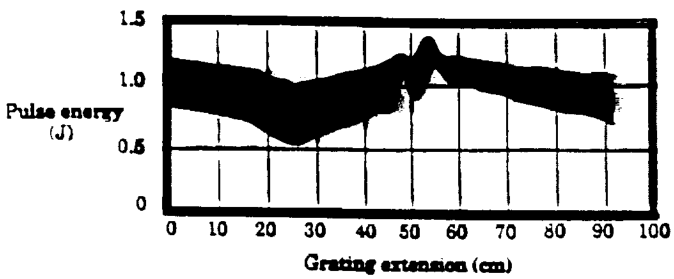

Figure 6: Pulse energy dependence upon grating extension.

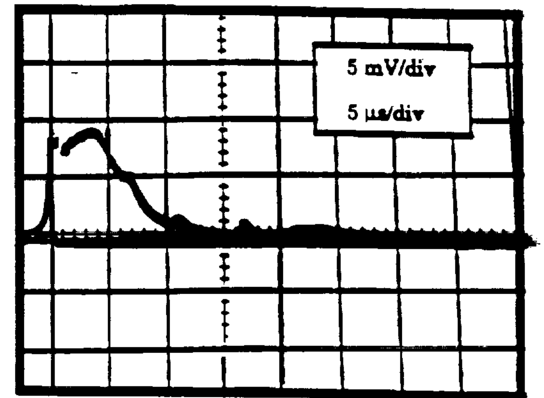

Figure 7: Pulse temporal profile after modification.

tuated in power. For extensions beyond 75 cm it became impossible to fill the output pattern despite adjustment to the grating.

During these adjustments we found that rotating the grating by 90° decreased the output energy by 50–75%. We also rotated the output coupler by 45° and found that the spatial output pattern degraded severely. We feel this is due to diffraction and polarization effects caused by the sharp edges of the square reflector. We will address both of these phenomena in more detail in future work.

When the lens L1 was replaced with a flat uncoated NaCl window the laser operated with a stable output energy and spatial distribution. The energy however decreased by 50%. We feel this is accounted for by the lack of A.R. coatings and the marginal quality of the substrate available at that time. The increased diffraction losses resulting from the use of a flat window may prove to be sufficient to cause stable operation without grating extension.

Matrix Method LP-140 Model

A MathCad^{TM} version 2.5 document is presented in Appendix A and may be used without alteration. The matrix technique used is taken from Siegman[10].

From this document, it can be seen that the extended cavity has a magnification of 2.0 and an equivalent Fresnel number of 1.7. On extending the cavity by 0.56 m and by changing the value of D2 in the document, the magnification is increased to 2.1 and the equivalent Fresnel number changes to 1.6. This implies that the improved mode stability is due to combination of increased diffraction losses and slightly improved Fresnel number.

CHARACTERISTICS OF THE MODIFIED LASER

Pulse Energy

The pulse energy was immediately observed to have increased slightly and stabilized. At the most stable point for pulse to pulse repeatability, the energy is equal to the original performance of 1 J/pulse. When the cavity length is slightly modified from this point by an extension of 2–5 cm, the energy increases by 10–15%. The spatial profile however is not quite as stable.

The optimum point of operation is better described as a window about 11 cm wide peaked at a cavity length extended by 56 cm.

Temporal Profile

The temporal profile at the peak cavity length improves substantially (Fig. 7). The pulse length not only shortens, but the tendency for multi-pulsing is also reduced.

At the original cavity length, inconsistent pulse lengths up to 12 μs were not uncommon with triple spikes in the pulse. By extending the cavity, these pulses have been reduced to 5–8 μs with a single well defined spike. It is important to note that at all cavity spacings, the gas mixture and pressure also play an important role in defining the temporal profile.

Spatial Profile

The spatial profile at the optimal cavity spacing demonstrates the most significant improvement (Fig. 8). Outside of the 11 cm window the profile is chaotic and exhibits strong beam pointing instabilities. Within the window the temporal profile fills out and the beam settles down to a high degree of stability.

It is difficult to quantify the exact nature of the spatial mode. The center obscuration creates a square output beam with a square hole in the center. The far-field

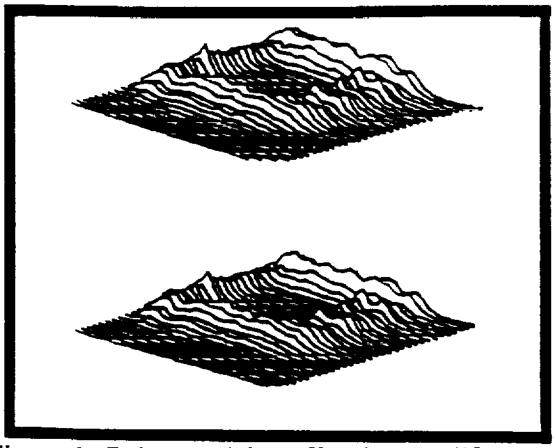

Figure 8: Pulse spatial profile after modification.

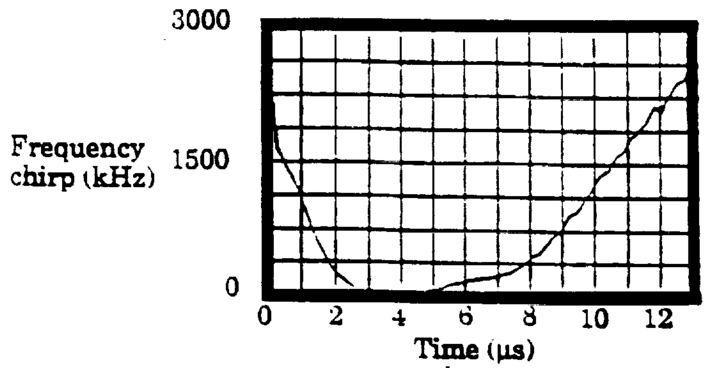

Figure 9: Frequency chirp.

diffraction pattern is non-uniform and may not be adequately described as gaussian or top-hat. Both the near and far-field patterns display large amounts of diffraction ripple.

Frequency Chirp

The chirp data was taken for pressures of 30–50 torr and was found to be stable and repeatable with a dependence on pressure. The higher pressure range from 40–50 torr provided the best results. The frequency chirp is shown in Figs. 9 and 10. The initial large downsweep in frequency can be attributed to the decaying electron density in the discharge[7] while the upswing is the conventional t^3 time dependence[8]. It can be seen that the pulse is approximately 13 μs long compared to the apparent 5 μs in the pulse temporal profile. This apparent difference is caused by the heterodyne technique which extracts the long, very low energy tail of the pulse from noise. Over this total pulse the frequency chirp is approximately 3 MHz. In practice the latter portion of the pulse is insignificant to the application and can be ignored. It can be seen from Fig. 10 that there is a 5 μs long portion of the pulse with approximately 250 kHz of chirp which is acceptable for our application. It should be possible to eliminate the leading and tail edge of the pulse to provide a slice which would contain 70% of the pulse energy.

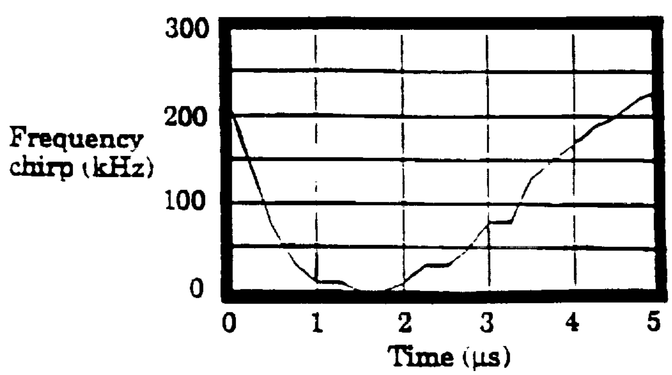

Figure 10: Frequency chirp.

Discharge Characteristics

Each of the discharges is driven by a separate circuit (Fig.11), although they are all switched by a common EG&G HY1102 thyratron. The discharge voltage pulse was measured using a Tektronics P6015 high voltage probe and the current pulse using a Pearson Electronics Model 110 induction coil. Both were connected to a LeCroy 9450 digitizing oscilloscope which downloaded the signal pulses to an IBM PC compatible computer for analysis. Typical current and voltage pulses for one

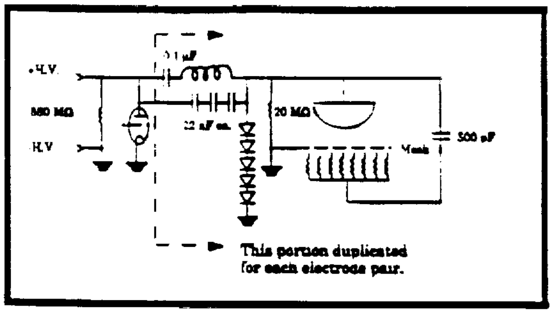

Figure 11: Sympathetic discharge circuit.

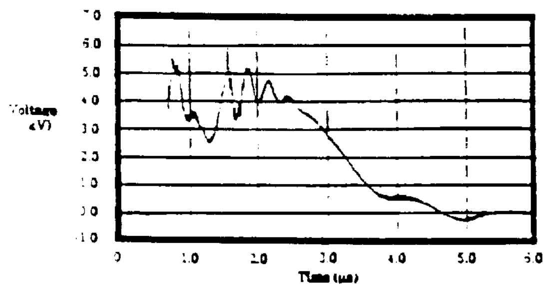

Figure 12: Voltage pulse.

of the electrodes are shown in Figs. 12 and 13. It can be seen that there is considerable ringing on the voltage pulse, which is due to a mismatch in the impedance of the discharge circuit and the laser discharge.

The electrical energy into the discharge can be obtained by integrating the voltage and current pulses (Fig. 14). This shows that the energy deposited into a single discharge is ≈3.5 J. However, only the energy deposited into the $CO_2(001)$ and the $N_2(\nu = 1-8)$ vibrational energy levels is useful for lasing action. Lowke et al.[9] have shown that the optimum excitation of these vibrational levels occurs for a reduced electric field or E/N of $\approx 1-3 \cdot 10^{-16}$ Vcm^2. The value of E/N was derived from the discharge voltage pulse form for each digitization interval together with the energy input in that interval. This enabled the

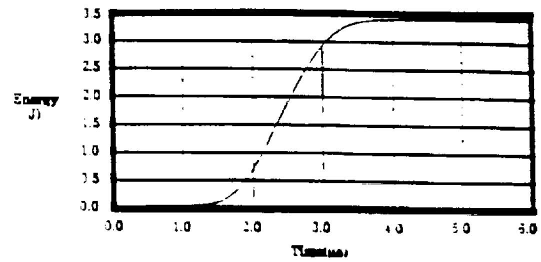

Figure 14: Energy over time.

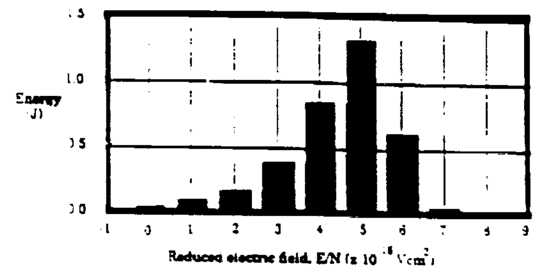

Figure 15: Energy input.

input energy into the discharge to be evaluated as a function of E/N for E/N intervals of $1 \cdot 10^{-16}$ Vcm^2 (Fig. 15). It can be seen that most of the energy is deposited in the $4-6 \cdot 10^{-16}$ Vcm^2. This results in the low laser efficiency of ≈4% compared to ≈12% for the laser in its original multimode long pulse configuration. This means that the discharge circuit requires optimizing for the new gas mixture. The evolution of the discharge impedance with time was found by dividing the voltage by the current (Fig. 16). It can be seen that the discharge impedance during the bulk of the energy input varies between 5 Ω and 20 Ω. This enables the discharge circuit to be optimized.

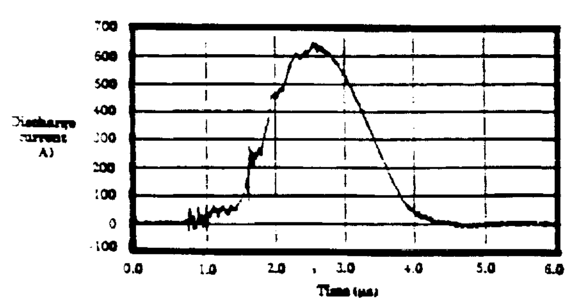

Figure 13: Current pulse.

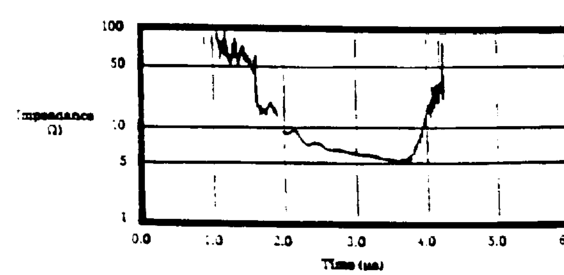

Figure 16: Discharge impedance.